1 **Modeling the Formation and Composition of Secondary Organic**
2 **Aerosol from Diesel Exhaust Using Parameterized and Semi-Explicit**
3 **Chemistry and Thermodynamic Models**

5 Sailaja Eluri[1], Christopher D. Cappa[2], Beth Friedman[3], Delphine K. Farmer[3], and Shantanu H. Jathar[1]
6 [1] Department of Mechanical Engineering, Colorado State University, Fort Collins, CO, USA, 80523
7 [2] Department of Civil and Environmental Engineering, University of California Davis, Davis, CA, USA, 95616
8 [3] Department of Chemistry, Colorado State University, Fort Collins, CO, USA, 80523
9 Correspondence to: Shantanu H. Jathar (shantanu.jathar@colostate.edu)

11 **Abstract**

12 Laboratory-based studies have shown that combustion sources emit volatile organic compounds that can be photo-oxidized in

13 the atmosphere to form secondary organic aerosol (SOA). In some cases, this SOA can exceed direct emissions of primary

14 organic aerosol (POA). Jathar et al. (2017) recently reported on experiments that used an oxidation flow reactor (OFR) to

15 measure the photochemical production of SOA from a diesel engine operated at two different engine loads (idle, load), two fuel

16 types (diesel, biodiesel) and two aftertreatment configurations (with and without an oxidation catalyst and particle filter). In

17 this work, we used two different SOA models, the volatility basis set (VBS) model and the statistical oxidation model (SOM),

18 to simulate the formation and composition of SOA for those experiments. Leveraging recent laboratory-based

19 parameterizations, both frameworks accounted for a semi-volatile and reactive POA; SOA production from semi-volatile,

20 intermediate-volatility and volatile organic compounds (SVOC, IVOC and VOC); multigenerational gas-phase chemistry; and

21 kinetic gas/particle partitioning. Both frameworks demonstrated that for model predictions of SOA mass to agree with

22 measurements across all engine load-fuel-aftertreatment combinations, it was necessary to model the kinetically-limited gas-

23 particle partitioning in OFRs as well as account for SOA formation from IVOCs, which were found to account for more than

24 90% of the model-predicted SOA. Accounting for IVOCs however resulted in an under-prediction of a factor of two for OA

25 atomic O:C ratios. Model predictions of the gas-phase organic compounds (resolved in carbon and oxygen space) from the

26 SOM compared favorably to gas-phase measurements from a Chemical Ionization Mass Spectrometer (CIMS), substantiating

27 the semi-explicit chemistry captured by the SOM. Model-measurement comparisons were improved on using vapor wall-loss

28 corrected SOA parameterizations. As OFRs are increasingly used to study SOA formation and evolution in laboratory and field

29 environments, models such as those developed in this work can be used to interpret the OFR data.

31 **1 Introduction**

32 Combustion-related aerosols are an important contributor to urban and global air pollution and have impacts on climate

33 (Pachauri et al., 2014) and human health (Anderson et al., 2012). While direct particle emissions from combustion sources are

34 dominated by primary organic aerosol (POA) and black carbon (Bond et al., 2004), these sources also emit more volatile

35 organic compounds (VOCs) that can photochemically react in the atmosphere to form secondary organic aerosol (SOA)

36 (Robinson et al., 2007). SOA production from combustion emissions is poorly understood and not very well represented in

37 models in terms of its precursors, gas-particle partitioning, composition, and properties (Fuzzi et al., 2015). Atmospheric

38 models frequently under-predict SOA mass concentrations during strong photochemical episodes in urban areas (Jathar et al.,

39 2017b), which likely highlights the challenge in modeling the SOA contributions from urban, combustion-related emissions

40 (Ensberg et al., 2014).

41

42 Diesel-powered sources, which are an important source of air pollution at urban and regional scales, emit precursors that form

43 SOA in the atmosphere (Gentner et al., 2016). Robinson et al. (2007) found that photochemical processing of exhaust

44 emissions from a small off-road diesel engine led to SOA production and doubled the primary aerosol mass over a few hours in

45 a chamber. Chirico et al. (2010) and Gordon et al. (2014) performed similar chamber experiments on tailpipe emissions from

46 in-fleet, on-road diesel vehicles run on chassis dynamometers. Both found SOA production that was roughly consistent with

47 the findings from Robinson et al. (2007). They additionally found that the use of aftertreatment devices (diesel oxidation

48 catalysts and diesel particulate filters) substantially reduced SOA production (mimicking the reduction in primary aerosol

49 emissions) but observed some SOA production during cold starts and/or regeneration events when the proper functioning of the

50 aftertreatment devices was limited. Furthermore, Gordon et al. (2014) found negligible differences in the SOA formation

51 between diesel and biodiesel fuel. To access longer equivalent photochemical aging timescales compared to typical chamber

52 experiments, Tkacik et al. (2014) measured SOA formation using an oxidation flow reactor (OFR) from air sampled from a

53 highway tunnel in Pittsburgh, PA used by both on-road gasoline and diesel vehicles. OFRs use high concentrations of

54 atmospheric oxidants, e.g. hydroxyl radicals, to achieve long exposures on short actual timescales; further discussion is

55 provided below. Tkacik et al. (2014) measured much stronger SOA formation compared to chambers (SOA: POA was 10:1)

56 over photochemical exposures equivalent to 2 to 3 days, but found that the SOA was lost, or destroyed, as the mixture

57 continued to age over the timescale of a week. Recently, Jathar et al. (2017a) performed experiments using an oxidation flow

58 reactor to measure the photochemical production of SOA from an off-road diesel engine operated at various engine load, fuel,

59 and aftertreatment configurations. Jathar et al. (2017a) found that efficient combustion at higher engine loads and removal of

60 SOA precursors by aftertreatment systems reduced SOA production by factors of 2 to 10. The only exception was that the

61 aftertreatment system did not seem to reduce SOA production at idle loads possibly because the exhaust temperatures were low

62 enough to limit removal of SOA precursors in the oxidation catalyst. Overall, these studies indicate that diesel exhaust

63 contributes to atmospheric SOA production, although the precise production of SOA varies across dimensions of

64 photochemical age, engine duty cycle, use of alternative fuels, and aftertreatment devices.

65

66 Oxidation flow reactors are being used to study the photochemical production of SOA from both anthropogenic (e.g., Ortega et

67 al. (2016)) and natural (e.g., Palm et al. (2016)) sources. Most OFRs used for SOA studies are 10 to 15 L, flow-through metal

68 reactors with lamps that can produce high concentrations of atmospheric oxidants to simulate photochemical processing (e.g.,

69 Lambe et al. (2011)). Flows through an OFR allow for residence times between one and three minutes, but given the high

70 oxidant concentrations OFRs can simulate up to two weeks of photochemistry. OFRs have three distinct advantages over

71 environmental chambers. First, OFRs are smaller in size and easier to operate than environmental chambers, which allows for

72 shorter experiments and makes them ideal for field deployments (Palm et al., 2016;Simonen et al., 2017). Second, production

73 of high oxidant concentrations in OFRs allows for much longer photochemical exposures (~factor of 10) than those possible

74 with chambers (Lambe et al., 2011). Third, due to their flow-through nature, OFRs have shorter residence times than

75 conventional chambers (~1-3 minutes) and hence are less susceptible to gas and particle losses that can influence SOA

76 formation (Zhang et al., 2014;Krechmer et al., 2016). Despite those advantages, there are concerns that the accelerated

77 chemistry and limitations to gas/particle partitioning may affect the formation and composition of SOA in OFRs, which calls

78 into question their relevance in understanding SOA formation in the real atmosphere (Palm et al., 2016;Jathar et al., 2017a).

79 For example, short residence times and/or small condensation sinks from preexisting aerosol may not allow for complete

80 condensation of SOA vapors (Lambe et al., 2015). Similarly, high oxidant concentrations in OFRs may lead to molecules

81 undergoing a greater number of reactions in the gas-phase before condensing, including reactions that lead to fragmentation

82   and formation of higher volatility products (Kroll et al., 2009). Both effects will typically suppress SOA production. With the

83   increased use of OFRs, there is a need to develop and use modeling tools that can account for fragmentation reactions and

84   kinetic gas/particle partitioning. This will allow for a more accurate interpretation of OFR data and facilitate translation of OFR

85   results to the real atmosphere.

86

87   Models used to simulate the photochemical production of SOA from VOCs in combustion emissions have traditionally used

88   the two-product (Odum et al., 1996) or the more generalized n-product volatility basis set (VBS) framework (Donahue et al.,

89   2006a). In this framework, VOC oxidation products are lumped into volatility bins based on their effective saturation

90   concentrations (C^*) and where the saturation concentration determines the partitioning of the products between the gas and

91   particle phases (Pankow, 1994). This framework has been widely used in both box (Dzepina et al., 2009;Hodzic et al.,

92   2010;Jathar et al., 2014a;Hayes et al., 2015) and three-dimensional (Murphy and Pandis, 2009;Tsimpidi et al., 2009;Jathar et

93   al., 2011;Ahmadov et al., 2012;Konovalov et al., 2015) models to simulate the chemistry and gas/particle partitioning of SOA.

94   While this framework offers a simple and computationally efficient scheme to model SOA formation, the use of volatility

95   alone neither tracks the molecular composition, nor informs the continued multi-generational chemistry that will determine the

96   atmospheric evolution and properties of SOA. As a result, volatility-based models have been challenged in leveraging

97   observations of the elemental composition of SOA (e.g., atomic O:C ratios) that have become possible through the use of the

98   aerosol mass spectrometer (AMS) to constrain parameterizations or test model predictions. Further, most volatility-based

99   models have employed *ad hoc* parameterizations to model multi-generational chemistry that do not account for fragmentation

100   reactions (Robinson et al., 2007) and possibly double count SOA formation (Jathar et al., 2016). Therefore, there is a demand

101   to develop models that can provide an improved representation of the chemistry that governs the formation, composition, and

102   properties of SOA.

103

104   Previously, volatility-based SOA models have been used to predict photochemical production of SOA from motor vehicle

105   exhaust (Robinson et al., 2007;Jathar et al., 2014b;Tkacik et al., 2014). These modeling studies have shown that speciated SOA

106   precursors such as long alkanes (C_{6-12}) and single-ring aromatics (e.g., benzene, toluene) explain less than 20% of the observed

107   SOA and have argued that the remainder of the SOA (~80%) arises from the photooxidation of typically unspeciated organic

108   compounds. These unspeciated compounds, also referred to as intermediate volatility organic compounds (IVOCs), are likely

109   species with carbon numbers larger than 12 and appear as an unresolved complex mixture on using traditional gas

110   chromatography mass spectrometry (GC-MS) techniques (Presto et al., 2011). Early estimates of IVOC emissions and their

111   SOA potential have significantly improved predictions of the SOA formed from diesel exhaust (Jathar et al., 2014b) and have

112   broadly improved OA model performance in three-dimensional large-scale models (Murphy and Pandis, 2009;Pye and

113   Seinfeld, 2010;Jathar et al., 2011;Tsimpidi et al., 2009). Consider as an example that Zhao et al. (2015), using a thermal

114   desorption GC-MS to provide detailed speciation of the carbon-number resolved linear, branched, and cyclic alkane IVOCs in

115   diesel exhaust, found that these species accounted for up to 60% of the non-methane organic gas emissions. While IVOCs have

116   been recognized as an important class of SOA precursors for diesel (and even for gasoline and biomass burning) sources,

117   updated emissions and speciation estimates from Zhao et al. (2015) have not yet been used to explain observations of

118   photochemically produced SOA from diesel exhaust.

119

120   Recently, several model frameworks have been developed to improve the representation of SOA formation, considering

121   dimensions of SOA beyond just volatility. The statistical oxidation model (SOM) developed by Cappa and Wilson (2012) is

122   one such example, although volatility remains an important consideration. The SOM is a semi-explicit, parameterizable

123   mechanism that uses a two-dimensional carbon-oxygen grid to simulate the multigenerational chemistry and gas/particle

124   partitioning of organic compounds. Although the SOM does not explicitly track or specify the product species composition

125   (e.g., functional groups), the carbon- and oxygen-number representation provides adequate detail to represent many key

126   atmospheric processes, e.g., reactions with oxidants, formation of functionalized products, scission of carbon backbones or

127   fragmentation, surface and condensed-phase chemistry and gas/particle partitioning. The SOM has been used to interpret

128   chamber experiments (Zhang et al., 2014;Cappa et al., 2013;Cappa and Wilson, 2012) and was recently integrated into a

129   chemical transport model (Jathar et al., 2015) to examine the influence of multigenerational aging (Jathar et al., 2016) and

130   chamber-based vapor wall losses (Cappa et al., 2016) on ambient concentrations and properties of OA. The two-dimensional

131   VBS (2D-VBS) of Donahue et al. (2011) and the carbon-polarity grid of Pankow and Barsanti (2009) are examples of similar

132   frameworks. These more sophisticated models (SOM, 2D-VBS, carbon-polarity grid) have not yet been employed to study

133   SOA formation from complex mixtures such as combustion emissions.

134

135   To summarize, combustion sources such as diesel-powered sources emit precursors that can photooxidize in the atmosphere to

136   produce SOA. This SOA production is dependent not only on the precursor composition (that could vary by combustion mode

137   and fuel type) and photochemical age, but also experimental artifacts (e.g., short condensation timescales) introduced by

138   oxidation flow reactors. Hence, there is a need to develop and apply sophisticated, yet computationally efficient, numerical

139   models to simulate and study SOA formation from combustion emissions. In this work, we applied two SOA model

140   frameworks that vary in sophistication (VBS and SOM) to simulate the photochemical production of SOA in an OFR from

141   diesel exhaust. The models were evaluated by comparing model predictions (OA and O:C) to the recent measurements made

142   by Jathar et al. (2017a) where SOA production was quantified for different photochemical ages under varying engine loads,

143   fuels, and aftertreatment devices. The model-measurement comparison, along with sensitivity simulations, highlights the

144   importance of modeling the kinetic gas/particle partitioning of SOA in OFRs, the contribution of IVOCs to the total SOA

145   production, and the ability of the SOM to accurately track the composition of SOA.

146

147   **2 Methods**

148   **2.1 Experiments and Data**

149   Jathar et al. (2017a) performed photooxidation experiments using an OFR to measure SOA production from the exhaust of a

150   4.5L, John Deere diesel engine. The stock engine met Tier 3 emissions standards for off-road diesel engines. The OFR used

151   therein was described in detail by Friedman et al. (2016) and the experimental setup and OA measurements from these

152   experiments were described in detail by Jathar et al. (2017a). We briefly summarize the experimental setup, measurements, and

153   findings from Jathar et al. (2017a). Diesel exhaust was diluted by a factor of 45-110 before entering the OFR. The intensity of

154   the mercury lamps (at wavelengths of 185 and 254 nm) inside the OFR was varied to produce different hydroxyl radical (OH)

155   concentrations and simulate different photochemical exposures. A suite of instrumentation was used to measure gas- (CO_2, CO,

156   total hydrocarbons, NO_x, O_2, oxygenated organic compounds) and particle- (aerosol size and composition) phase

157   concentrations. A total of fourteen experiments (see Table 1 for more details) were performed at varying engine loads and with

158   varying fuels and aftertreatment configurations. The OH exposure was varied between 0 and a maximum of 9.2×10^7

159   molecules-hr cm^{-3} (equivalent to 2 days of photochemical aging at an OH concentration of 1.5×10^6 molecules cm^{-3}). On

160   average, each experiment included measurements at six to seven different photochemical exposures. The mass concentrations

161   and elemental composition of the POA (measured when OFR lights were off) and SOA (at varying OH exposures) were

162   measured by a high-resolution aerosol mass spectrometer (HR-AMS). In addition to the measurements reported by Jathar et al.

163   (2017a), the gas-phase concentrations of oxygenated organic compounds were measured by an acetate reagent ion-based

164   chemical ionization mass spectrometer (CIMS) (Link et al., 2016). At all engine configurations, SOA production exceeded the

165   POA emissions after the equivalent of a few hours of atmospheric photochemical aging. SOA production was particularly

166   strong at idle (or less fuel-efficient) engine loads and/or when exhaust temperatures were low and proper functioning of the

167   aftertreatment devices was limited. Further, POA emissions and SOA production were nearly identical between diesel and

168   biodiesel fuels. A synopsis of the THC (which includes all SOA precursors), POA, SOA, O:C, OH, and size distribution data

169   are presented in Table 1.

170

171   **2.2 Organic Aerosol Models**

172   In this work, we used two different OA models to predict the mass concentrations and chemical composition of SOA and

173   compare predictions against the SOA measurements from Jathar et al. (2017a) and Friedman et al. (2017). In this section, we

174   briefly describe the two model frameworks, namely the Volatility Basis Set (VBS) and the Statistical Oxidation Model (SOM),

175   used to simulate the coupled chemistry, thermodynamic properties, and kinetic gas/particle partitioning of OA. The VBS model

176   was chosen as it is widely used in contemporary air quality models; the SOM was chosen to examine the influence of improved

177   representation of OA processes (e.g., fragmentation reactions) on model predictions.

178

179   **2.2.1 Volatility Basis Set**

180   The Volatility Basis Set model, developed by Donahue et al. (2006b), is a parameterizable model that allows for a volatility-

181   based representation of the coupled chemistry, thermodynamic properties, and gas/particle partitioning of OA. The VBS uses

182   logarithmically spaced so-called basis sets based on the effective saturation concentration (C^*); C^* of a species determines the

183   partitioning between the gas and particle phases (Pankow, 1994). In the VBS model, precursor VOCs were allowed to react

184   with OH to yield a unique product distribution in C^* space that represented stable first-generation products. Subsequent multi-

185   generational gas-phase oxidation, or so-called 'aging,' of the VBS products was modeled using the scheme of Robinson et al.

186   (2007). In this scheme the product species are allowed to react with OH and yield a product with a C^* that was an order of

187   magnitude lower than the direct precursor, to a lower limit C^* of 10^{-1} µg m^{-3}. This scheme did not consider fragmentation

188   reactions. The following equations were used to represent the precursor VOC oxidation (equation 1) and subsequent reaction

189   and formation of products from VOC oxidation and aging reactions (equation 2):

190    $$\frac{dV}{dt} = -k_{OH}[V][OH] \tag{1}$$

191    $$\frac{dC_j^{g+p}}{dt} = \alpha_j k_{OH}[V][OH] + \beta\, k_{OH,aging}[C_{j+1}^g][OH] - \gamma\, k_{OH,aging}[C_j^g][OH] \tag{2}$$

192   where V is the gas-phase concentration of a generic VOC precursor (µg m^{-3}; here, VOC includes VOCs, IVOCs and SVOCs),

193   k_{OH} is the reaction rate constant between the VOC and OH (cm^3 molecule^{-1} s^{-1}), C_j^{g+p} is the gas + particle-phase concentration

194   in the jth bin (µg m^{-3}), α_j is the mass yield of the first-generation oxidation product of the jth bin (Table 2), $k_{OH,aging}$ is the reaction

195   rate constant (cm^3 molecule^{-1} s^{-1}) to represent multi-generational aging of the oxidation products, and β and γ are the mass

196   yields associated with the production and loss terms from multi-generational aging. For the jth bin, the second term in equation

197   (2) represents the formation of oxidation products from the $j+1^{th}$ volatility bin and the third term in equation (2) represents the

198   loss of precursor from the jth bin. β and γ are assumed to have a value of 1 (meaning no fragmentation) but β is zero for the last

199   bin and γ is zero for the first bin.

200

201 Volatility-resolved mass yields for eighteen different VOCs for C^* bins ranging from 10^{-1} to 10^3 µg m^{-3} were adopted or refit

202 based on parameterizations published in the literature; VOCs, their VBS mass yields, and the relevant references are listed in

203 Table 2. Some of these parameterizations accounted for vapor wall losses and have been accordingly marked in Table 2. Each

204 SOA precursor in the exhaust emissions was assigned a surrogate from Table 2 to model SOA formation in the VBS model.

205 Branched and cyclic alkanes were assigned surrogates based on equivalent linear alkanes, following the work of Lim and

206 Ziemann (2009) and Tkacik et al. (2012). A C_X branched alkane was assigned a C_{X-2} linear alkane as a surrogate and a C_X

207 cyclic alkane was assigned a C_{X+2} linear alkane as a surrogate. Since we only fit alkanes up to n-heptadecane, we considered n-

208 heptadecane as a surrogate for alkanes C_{17}-C_{22}. The mass transfer (condensation/evaporation) of the VBS products to the

209 particle phase was assumed to be kinetically-limited in the OFR (Palm et al., 2016;Jathar et al., 2017a); Section 2.3 describes

210 the mass transfer equation used to model kinetic gas/particle partitioning.

211

212 **2.2.2 Statistical Oxidation Model**

213 The Statistical Oxidation Model (SOM), developed by Cappa and Wilson (2012) is a semi-explicit, parameterizable model that

214 allows for a statistical representation of the coupled chemistry, thermodynamic properties, and gas/particle partitioning of OA.

215 The SOM uses a 2-dimensional carbon-oxygen grid to track gas- and particle-phase precursors and products from VOC

216 oxidation. Each cell in the SOM grid represents a model organic species with a molecular weight defined by the formula

217 $C_xH_yO_z$. A SOM species reflects the average properties (e.g. C^*, reactivity) of all actual species with the same number of

218 carbon (N_C) and oxygen (N_O) atoms that are produced from a given precursor class (e.g., benzene, alkanes). In the SOM, all

219 gas-phase species are assumed to be reactive towards OH and the OH reactivity (k_{OH}) is calculated using equation 3 as follows:

220 $$log(k_{OH}) = A_1 + A_2 \times (N_C^{As}) \times exp(-1 \times \frac{E_a}{8.314 \times T}) \times [1 + \frac{b_1}{\sigma\sqrt{2\pi}} exp(-\frac{1(ln(N_O+0.01)-ln(b_2)^2}{2\sigma^2})] \quad (3)$$

221 $\sigma (N_C \leq 15) = 0.0214 \times N_C + 0.5238$

222 $\sigma (N_C \geq 15) = -0.115 \times N_C + 2.695$

223 $b_1 = -0.2583 \times N_C + 5.8944$

224 $b_2 (N_C \leq 15) = 0.0314 \times N_C + 0.9871; \ b_2 (N_C > 15) = 0.25 \times N_C - 2.183$

225 where A_1=15.1, A_2=3.94, and A_3=0.797. k_{OH} for a specified N_C and N_O is assumed to be the same for species in all the SOM

226 grids.

227

228 The reactions with OH lead to either functionalization or fragmentation, resulting in movement through the carbon-oxygen

229 grid. Six precursor-specific adjustable parameters are assigned for each SOM grid: four parameters that define the molar yields

230 of the four functionalized, oxidized products ($p_{O,k}$, $\Sigma p_{O,k}$=1 and hence one out of the four parameters is determined by mass

231 balance), one parameter that determines the probability of functionalization or fragmentation (P_{Frag}, P_{Func}=1-P_{Frag}) and one

232 parameter that describes the change in C^* associated with the addition of one oxygen atom (ΔLVP). Equation 4 represents the

233 evolution of species in the SOM grid:

234 $$\frac{d[C_XO_Z]}{dt} = -k_{OH}^{X,Z}[OH][C_XO_Z] + [OH]\sum_{k=1}^{4} k_{OH}^{X,Z-k} P_{func}^{X,Z-k} p_{O,k}[C_XO_{Z-k}] +$$

235 $$[OH]\sum_{j=1}^{jmax}\sum_{k=0}^{kmax-Z} k_{OH}^{X+j,Z-1+k} \frac{P_{frag}^{X,Z-1+k}}{N_{fragments}^{X,Z}}[C_XO_{Z-1+k}] \quad (4)$$

236 where C_XO_Z is the gas + particle-phase concentration of the SOM species with X carbon atoms and Z oxygen atoms (µg m^{-3})

237 and $N_{fragments}$ is the number of possible products from fragmentation. The probability of fragmentation is modeled using

238   equation 5 as a function of the O:C ratio because higher O:C ratio compounds are expected to have a higher probability of

239   fragmentation (Chacon-Madrid and Donahue, 2011):

240    $P_{frag} = \left(\frac{N_O}{N_C}\right)^{m_{frag}}$ (5)

241   The C^* for each SOM species was calculated using equation 6 as follows:

242    $log_{10}C^* = -0.337 MW_{HC} + 11.56 - (N_O \times \Delta LVP)$ (6)

243   where MW_{HC} (g mole[-1]) is the molecular weight of the hydrocarbon backbone (accounting only for the carbon and hydrogen

244   atoms).

245

246   The parameters used to model SOA formation were based on those published in Cappa et al. (2016) and are listed in Table 3.

247   These parameter sets were developed by fitting the SOM predictions to chamber measurements of SOA mass concentrations

248   and include corrections to account for vapor wall losses (Zhang et al., 2014). Each SOA precursor in the exhaust emissions was

249   assigned a surrogate from Table 3 to account for the oxidation chemistry associated with oxidation of that species. For

250   example, pentadecane used the parameterization developed by fitting *n*-dodecane. The difference in the initial number of

251   carbons and oxygens, and thus the volatility, between the surrogate compound and the precursor compound of interest was

252   accounted for, with consequent impact on the SOA yield. In other words, unlike the VBS where the SOA mass yield of the

253   SOA precursor and surrogate is identical, the surrogate in the SOM only informed the statistical trajectory for multi-

254   generational oxidation of a given precursor, and the surrogate and actual compound of interest can have different SOA mass

255   yields. Similar to the VBS model, the mass transfer (condensation/evaporation) of the SOM products to the particle phase was

256   assumed to be kinetically-limited in the OFR (Palm et al., 2016;Jathar et al., 2017a) and Section 2.3 below describes the mass

257   transfer equation used to model kinetic gas/particle partitioning.

258

259   **2.3 Kinetic Gas/Particle Partitioning**

260   Palm et al. (2016) and Jathar et al. (2017a) have argued that the short residence times and small condensation sinks in the OFR

261   may not permit all low-volatility products formed from VOC oxidation to condense onto preexisting aerosol. Hence, unlike

262   earlier work that has assumed equilibrium partitioning to model SOA in OFRs (Tkacik et al., 2014;Chen et al., 2013), we

263   modeled the kinetic gas/particle partitioning of OA using equation 7 (Zhang et al., 2014):

264    $\frac{dc_i^p}{dt} = 2\pi D_i D_p N_p F_{FS}\left(C_i^g - \frac{c_i^p C_i^*}{C_{OA}}\right)$ (7)

265   where C_i^p is the particle-phase mass concentration for the ith organic species (µg m^{-3}), D_i is the gas-phase diffusion coefficient

266   of the ith organic species (m[2] s^{-1}), D_p is the number mean particle diameter (m) , N_p is the total particle number concentration

267   (m[-3]), F_{FS} is Fuchs-Sutugin correction for non-continuum mass transfer, C_i^g is the gas-phase mass concentration of the ith

268   organic species (µg m^{-3}), C_i^* is the effective saturation concentration of the ith organic species, and C_{OA} is the total OA mass

269   concentration (µg m^{-3}). The ith organic species refers to the organic compounds tracked in the VBS bins and the SOM grids.

270   The gas-phase diffusion coefficient was calculated for each organic species as follows:

271    $D_i = D_{CO_2} \frac{MW_{CO_2}}{MW_i}$ (8)

272   where D_{CO_2} is the gas-phase diffusion coefficient of CO_2 (1.38×10^{-5} m[2] s^{-1}), MW_{CO_2} (g mole[-1]) is the molecular weight of CO_2,

273   and MW_i (g mole[-1]) is the molecular weight of the ith organic species. In the VBS model where we do not track the molecular

274   composition of the SOA species, we assumed all condensing species to have a molecular weight of 200 g mole[-1]. The Fuchs-

275   Sutugin correction was calculated as follows:

276 $\qquad F_{FS} = \frac{0.75\alpha(1+Kn)}{Kn^2 + Kn + 0.283 \cdot Kn \cdot \alpha + 0.75\alpha}$ $\qquad$ (9)

277 $\qquad Kn = \frac{2\lambda_i}{D_p}$ $\qquad$ (10)

278 $\qquad \lambda_i = \frac{3D_i}{C_j}$ $\qquad$ (11)

279 $\qquad C_i = \sqrt{\frac{8N_A kT}{\pi MW_i}}$ $\qquad$ (12)

280 where Kn is the Knudsen number, α is the mass accommodation coefficient, λ_i is the mean free path of the ith organic species in

281 air (m), C_i is the root mean square speed of the gas (m s^{-1}), N_A is Avogadro's number (molecules mole^{-1}), k is the Boltzmann

282 constant (m^2 kg s^{-2} K^{-1}), and T is the temperature (K).

283

284 **2.4 Model Inputs**

285 **2.4.1 Semi-Volatile and Reactive POA**

286 Previous work has shown that much of combustion-related POA is semi-volatile and exists in an equilibrium with gas-phase

287 vapors (Robinson et al., 2007;Huffman et al., 2009;May et al., 2013c, b;May et al., 2013a). Jathar et al. (2017a) measured

288 emissions of POA at no OH exposure and these measured concentrations were used to initialize the seed OA available for

289 partitioning in the OFR and to calculate the mass concentrations of vapors in equilibrium with the POA. The mass

290 concentrations of the POA vapors were determined based on the normalized, volatility-resolved distribution of primary organic

291 compounds estimated by May et al. (2013b) for emissions from a suite of on- and off-road diesel vehicles. The volatility

292 distribution of May et al. (2013b) for diesel primary organic compounds is listed in Table 4(a). For the SOM, we assumed that

293 the primary organic compounds could be represented using a distribution of *n*-alkanes and we refit the volatility distribution in

294 Table 4(a) to develop a carbon-number resolved distribution of *n*-alkanes; this distribution is listed in Table 4(b). The POA and

295 POA vapors estimated for the VBS and SOM models for all the experiments are listed in the supplementary information

296 (Tables S1 and S2).

297

298 **2.4.2 SOA Precursors**

299 Jathar et al. (2017a) did not speciate the THC or SOA precursor emissions from the diesel engine and hence we have developed

300 our own emissions profiles based on previously published literature to speciate the THC emissions. In this work, we used two

301 different emissions profiles listed in EPA SPECIATE version 4.3 that are commonly used to speciate THC emissions from

302 diesel engines for emissions inventories used in atmospheric modeling (EPA, 2013): Profiles #3161 (Diesel Exhaust- Farm

303 Equipment) and #8774 (Heavy Duty Diesel Exhaust). Profile #3161 best matched the diesel engine source and diesel fuel used

304 by Jathar et al. (2017a) and was used as the baseline emissions profile to speciate the THC emissions; we examined the

305 sensitivity of using Profile #8774 on model predictions. We were unable to find a comprehensive emissions profile for THC

306 emissions from the use of straight biodiesel fuel in the literature, and have relied on emissions profiles that were determined for

307 biodiesel-diesel blends. Profile #4777 (30% Biodiesel Exhaust - Light Duty) was used as the baseline emissions profile to

308 speciate THC emissions for experiments performed using the biodiesel fuel. All three emissions profiles (3161, 8774, and

309 4777) are listed in Tables S1 through S3.

310

311 Prior work in studying SOA formation has revealed that traditional speciation of THC emissions does not include emissions of

312 high molecular-weight organic compounds, such as IVOCs, that are important SOA precursors (Jathar et al., 2014b). In Profile

313 #3161 such compounds are partially accounted for in the 'unknown' species category (13.76% by mass of THC). Zhao et al.

314   (2015) recently estimated the magnitude of IVOCs in THC emissions from a suite of on- and off-road diesel engines and

315   provided a semi-explicit speciation of the IVOC emissions as a carbon-number distribution of linear, branched and cyclic

316   alkanes. To account for these IVOC emissions, we assumed that the baseline emissions profiles contained 60% IVOCs on a

317   mass-basis, based on the median estimate in Zhao et al. (2015), and had the same chemical speciation as that proposed by Zhao

318   et al. (2015) for an off-road engine (transportation refrigeration unit). We performed sensitivity simulations using IVOC

319   fractions of 0% (assuming that the THC emissions contained no IVOCs) and 13.76% (based on the 'unknown' category in

320   Profile #3161), on a mass-basis. Addition of IVOCs to the baseline emissions profile meant that the VOC species (e.g.

321   benzene, toluene, short alkanes) had to be renormalized to accommodate the IVOCs. Table 5 lists the renormalized baseline

322   emissions profiles for SOA precursors used for diesel and biodiesel exhaust with 60% IVOCs along with the reaction rate

323   constants with OH (k_{OH}) and surrogates (or model compound) used to model SOA formation for the VBS and SOM models.

324   Concentrations for each species were determined by multiplying the experiment-specific THC mass concentrations with the

325   renormalized emissions profile.

326

327   **2.4.3 Particle Size and Particle Number Concentrations**

328   For numerical simplicity, we used a monodisperse aerosol, the properties of which (number mean diameter (D_p) and number

329   concentration (N_p)) were initialized from the measured particle size distribution data when modeling kinetic gas/particle

330   partitioning. For experiments performed without the DPF+DOC, the initial particle number concentrations and condensational

331   sinks were high ($>3 \times 10^5$ # cm^{-3} and >0.5 min^{-1}) and hence the monodisperse aerosol was initialized based on data at no

332   photochemical exposure. For experiments performed with the DPF+DOC where the initial particle number concentrations were

333   relatively low (<1000 # cm^{-3} and <0.003 min^{-1}), photochemical aging resulted in formation and growth of new particles and

334   provided a substantial increase in the surface area ($>$factor of 100) available for condensation. In these experiments, we

335   initialized the monodisperse aerosol using an average of the data at no photochemical exposure and after photochemical

336   exposure (Palm et al., 2016). Averaging the data allowed for a more realistic estimate of the condensational sink. In each

337   simulation, the condensing SOA mass was used to calculate the change in particle size but the number concentration was

338   conserved. The number mean diameter and the number concentration data - representing the initial condensational sink – for all

339   experiments are listed in Table 1.

340

341   New particle formation and growth was observed for most experiments at or near the highest photochemical ages (at or >1 OH

342   day), which presumably influenced the condensational sink at the beginning of the experiment. Therefore, we performed

343   sensitivity simulations to investigate the influence of new particle formation on model predictions. We performed simulations

344   with each model (VBS and SOM) with four different initial condensational sinks. The first three simulations used measured

345   data to calculate the initial condensational sink inputs: (i) number mean diameter and measured number concentration at no OH

346   exposure (equivalent to the default for non-DPF+DOC experiments), (ii) number mean diameter and measured number

347   concentration at the given OH exposure, and (iii) average of (i) and (ii) (default for DPF+DOC experiments). The fourth

348   simulation (iv) assumed that the OFR nucleated 1 nm particles at the beginning of the experiment where the number

349   concentration of these particles was equal to that measured at the end of the experiment.

350

351   **2.5 Model Simulations and Model Code**

352   The VBS and SOM models were run separately for each photochemical exposure simulated for each experiment listed in Table

353   1. In the VBS simulations, POA was tracked in one basis set while products from each SOA precursor were tracked in separate

354 basis sets, allowing us to distinguish between POA and SOA. In the SOM simulations, all precursor molecules with the same

355 surrogate (e.g., all *n*-alkanes) were tracked in the same SOM grid. Model simulations were performed in phases to answer

356 specific questions and inform model inputs for later simulations:

357 1. To provide a general overview of the model predictions and model-measurement comparison, and to orient the reader

358 to the results thereafter, we performed simulations with the VBS and SOM models using the base set of inputs for one

359 of the Idle-Diesel-None experiments. Our base case included: Profile #3161 for VOC emissions, 60% IVOC mass

360 fraction, kinetic gas/particle partitioning with a mass accommodation coefficient of 0.1, and monodisperse aerosol

361 inputs based on measured data at no photochemical exposure.

362 2. Models used to simulate SOA production in environmental chambers and OFRs have typically assumed instantaneous

363 equilibrium partitioning (e.g., Chen et al. (2013)). To examine the validity of assuming instantaneous equilibrium

364 partitioning, we performed simulations with the VBS and SOM models using instantaneous or kinetic gas/particle

365 partitioning for one of the Idle-Diesel-None and the Idle-Diesel-DPF+DOC experiments. Kinetic partitioning was

366 modeled using three values of the mass accommodation coefficient (α=0.01, 0.1, 1) to capture the uncertainty in its

367 true value. To examine the influence of an increased initial condensational sink from new particle formation on kinetic

368 partitioning, we performed additional simulations using four different initial condensational sinks (see Section 2.4.3)

369 on one of the Idle-Diesel-None and the Idle-Diesel-DPF+DOC experiments.

370 3. Previous work has shown that combustion-related IVOCs are important precursors of SOA (e.g., Jathar et al. (2014b)).

371 To investigate the importance of IVOCs, we performed simulations with the VBS and SOM models at three different

372 assumed IVOC mass fractions (0%, 13.76%, and 60%), as discussed above when discussing the THC profiles, at all

373 photochemical exposures and for all the experiments listed in Table 1. We performed additional simulations with

374 different emissions profiles and SOA parameterizations on one of the Idle-Diesel-None experiments to further

375 investigate uncertainties linked to the composition and SOA potential of IVOCs.

376 4. Additional simulations were performed to examine the sensitivity of model predictions to the following processes:

377 multi-generational aging, vapor wall losses, residence time distributions, spatial heterogeneity in OH concentrations,

378 and low NO$_x$ SOA parameterizations.

379 The numerical codes for the VBS were developed in Matlab while those for the SOM were developed in IGOR (WaveMetrics

380 Inc.). These codes will be made available on request. The simulations were performed on an Intel i5 processor (1.7 GHz) and

381 required ~10 s to perform a VBS simulation and ~500 s to perform a SOM simulation at a single photochemical exposure.

382

383 **3. Results**

384 **3.1 General Model Results Using the Base Case**

385 We compare predictions of OA from the VBS and SOM models using the base case to the measurements in Figure 1 for the

386 Idle-Diesel-None experiment. Figures 1(a) and 1(b) compare predictions to the measurements in units of μg m^{-3} and g kg-fuel^{-1},

387 respectively; hereafter we present all mass predictions in units of g kg-fuel^{-1}. For this experiment, the VBS and SOM models

388 over-predicted the OA mass by a factor of ~3 at the lower photochemical exposures (0.06 and 0.17 OH days). For higher

389 photochemical exposures (>0.5 OH days), both models performed very well in reproducing the OA evolution with little

390 difference between the VBS and SOM models. Although our base case seemed to offer a reasonable model-measurement

391 comparison for this specific experiment, the model performance did vary across the suite of experiments, which is discussed in

392 more detail in Section 3.3. The VBS and SOM models predicted that the OA at the maximum photochemical exposure was

393 dominated by SOA produced from VOC and IVOC oxidation (94%), which agreed well with the measured composition (see

394   Figure 1(c)). For the measurements, POA was defined as fresh OA while SOA was defined as OA formed in addition to the

395   POA. Furthermore, both models suggested that most of the SOA emanated from the oxidation of IVOCs with only about 3-4%

396   resulting from the oxidation of aromatic VOCs and less than 1% resulting from alkane VOCs smaller than a C_{12}. This

397   dominance of IVOCs in explaining the photochemically produced SOA is in line with previous OFR and chamber studies that

398   have modeled SOA formation from diesel exhaust (Tkacik et al., 2014;Zhao et al., 2015;Jathar et al., 2014b).

399

400   **3.2 Kinetic Gas/Particle Partitioning**

401   In Figure 2, we plot predictions from the VBS and SOM models for the Idle-Diesel-None and Idle-Diesel-DPF+DOC

402   experiments assuming instantaneous and kinetic gas/particle partitioning. The two different experiments were deliberately

403   chosen to highlight the role instantaneous partitioning plays at the extremities. We found that for the Idle-Diesel-None

404   experiment, the use of instantaneous partitioning produced the same result as kinetic partitioning with α values of 0.1 and 1 and

405   that all these predictions resulted in roughly the same model-measurement comparison. The kinetic partitioning simulations

406   (except for that with an α of 0.01) produced the same result as the instantaneous partitioning simulation most likely because the

407   initial condensational sink was large enough (1.12 min^{-1}) in this experiment that there were no kinetic limitations to

408   partitioning. The increase in the condensational sink through condensation of SOA (10 min^{-1} at the highest photochemical

409   exposure) tended to further reduce any differences in the predictions between the kinetic and instantaneous partitioning

410   simulations. However, for the Idle-Diesel-DPF+DOC experiment, the instantaneous partitioning simulation predicted

411   substantial SOA production at the lower photochemical exposures (0.04 and 0.12 OH days) compared to the kinetic

412   partitioning simulations, specifically a factor of 10 to 100 larger for the VBS model and a factor of 3 to 4 larger for the SOM.

413   The instantaneous partitioning simulations predicted a lot more SOA because all condensable products of VOC oxidation were

414   allowed to condense instantaneously (according to their respective volatilities) while the kinetic partitioning simulations

415   predicted little SOA production because the initial condensational sink was quite small (0.002 min^{-1}). Predictions from the

416   instantaneous and kinetic partitioning simulations were nearly identical at the higher photochemical exposures because the

417   SOA formed had grown the condensational sink enough to reduce limitations to partitioning (10 min^{-1} at the highest

418   photochemical exposure). These results imply that the condensation of SOA in OFRs, at least to some extent, could be

419   kinetically-limited and that instantaneous partitioning may result in models over-predicting the condensation and formation of

420   SOA.

421

422   We make two additional observations based on the results in Figure 2. First, the initial condensational sink for the Idle-Diesel-

423   None experiment was large (1.12 min^{-1}) compared to condensational sinks one would encounter in the real atmosphere. For

424   example, 5 μg m^{-3} of aerosol in a representative rural or remote environment will have a condensational sink <0.05 min^{-1}

425   (Seinfeld and Pandis, 2006). Therefore, modeling ambient applications of the OFR will need to be even more mindful of the

426   instantaneous partitioning assumption while predicting SOA formation. Second, for the kinetic partitioning results, predictions

427   from both models were relatively insensitive to α values between 0.1 and 1 but were dramatically lower (factor of ~4) for an α

428   value of 0.01. Given the reasonable model-measurement comparison at an α value of 0.1 and 1, we argue that the SOA

429   condensation needs to be represented by an α value larger than 0.1 for the OFR experiments in this work. This α value for

430   diesel exhaust SOA is consistent with prior estimates of the α value of α-pinene SOA estimated from chamber and aerosol

431   heating experiments (Karnezi et al., 2014) (Lee et al., 2011;Saleh et al., 2013) but significantly higher than that observed

432   recently for toluene SOA under dry conditions (Zhang et al., 2014). Model results presented hereafter include a kinetic

433   treatment of gas/particle partitioning and assumed an accommodation coefficient of 0.1.

434

435 Results from model simulations performed using different initial condensational sink inputs, some of which captured the

436 influence of new particle formation, are plotted in Figure 3. We found that the initial condensational sink had no influence on

437 the OA predictions from both models for the Idle-Diesel-None experiment, despite substantial differences in the initial

438 condensational sink between the different cases. This was because the amount of SOA formed (875 µg m^{-3} at the highest

439 photochemical exposure) was sufficient to grow the condensational sink enough that the initial condensational sink did not

440 matter. In contrast, for both models we found large differences between the model predictions of OA for the Idle-Diesel-

441 DPF+DOC experiment. The use of inputs based on the measurements at no OH exposure, where the aftertreatment system

442 significantly reduced number concentrations (910 cm^{-3}) and hence the available condensational sink (0.0018 min^{-1}), produced

443 much less SOA (factor of ~3 lower) and poorer agreement with the measurements (see curve (i) in Figure 3). Initial

444 condensational sinks that captured the influence of new particle formation resulted in better agreement of the model predictions

445 with measurements. The DPF+DOC results also suggest that calculating an initial condensational sink using data from before

446 and after photochemical exposure could be used as an input to model OFR data.

447

448 **3.3 Influence of IVOCs on SOA Formation**

449 In Figure 4(a), we compare predictions of SOA concentrations from the SOM against measurements for all the experiments

450 listed in Table 1 and at all photochemical exposures. For visual clarity, we do not present results from the VBS model as both

451 models had nearly identical predictions with a few exceptions; see Figure S1 where we compare VBS model predictions to

452 SOM predictions for all experiments at all photochemical exposures for the base case. The three panels in Figure 4(a) show

453 model-measurement comparisons assuming three different fractions of IVOCs: 0%, 13.76% and 60%; statistical metrics of

454 fractional bias, fractional error, and R^2 for the comparison for both models are listed in Table S4. The model-measurement

455 comparison and the model skill was very poor when no IVOCs were included (fractional bias = -135%, fractional error =

456 146%, and $R^2 = 0.79$); this model reflects the treatment of diesel-powered sources in most traditional emissions inventories and

457 large-scale models. The model performance improved with 13.76% IVOCs (fractional bias = -60%, fractional error = 108%,

458 and $R^2 = 0.92$) and 60% IVOCs (fractional bias = 46%, fractional error = 87%, and $R^2 = 0.92$). The optimal model performance

459 that produced the lowest fractional bias and fractional error was realized at an IVOC mass fraction of 40% (fractional bias= -

460 10%, fractional error= 97%, and $R^2 = 0.9$) (not shown). For predictions with an IVOC mass fraction of 40%, 59% and 68% of

461 the model predictions were within a factor of 1.5 and 2 of the measurements. These comparisons indicate that it is critical that

462 IVOCs be included when modeling the SOA formation from diesel exhaust and also validate the IVOC emissions and

463 composition estimates made by Zhao et al. (2015) for IVOCs.

464

465 We further investigated the IVOC species that contributed the most to SOA formation. Cyclic alkane IVOCs accounted for

466 45% of the THC emissions and contributed 40 to 75% of the SOA formation across the different experiments. We should note

467 that the speciation of cyclic alkane IVOCs in Zhao et al. (2015), while robust in quantifying the carbon number, did not include

468 any specificity in terms of the molecular structure, i.e., their methods would not be able to distinguish between a pure C$_{10}$

469 cyclic alkane and a cyclohexane with a 4-carbon branch. Further, the parameterizations to model SOA formation from cyclic

470 alkane IVOCs for both models were based on the behavior of particular compounds. In the VBS model, the surrogate for a

471 cyclic alkane IVOC was determined through equivalence with a straight alkane IVOC while in the SOM the cyclic alkane

472 IVOCs were tied to parameterizations for hexylcyclohexane. (The observed SOA yield and derived SOM parameterization for

473 hexylcyclohexane is actually quite similar to that for cyclododecane for low-NO$_x$ conditions, but not for high-NO$_x$ conditions

474   (Cappa et al., 2013).) This lack of specificity in the speciation and the SOA parameterizations made the SOA predictions from

475   the oxidation of cyclic alkane IVOCs relatively uncertain. To examine the sensitivity of the model predictions to uncertainties

476   in the model treatment of cyclic alkane IVOCs, we performed simulations with both models for one of the Idle-Diesel-None

477   experiments where the cyclic alkane IVOCs were treated as branched alkane IVOCs; results from these simulations are shown

478   in Figure 5(a). The use of branched alkane IVOCs to model cyclic alkane IVOCs reduced OA predictions at the highest

479   photochemical exposure by 33% and 11% for the VBS and SOM models respectively, suggesting that the model predictions

480   were modestly sensitive to the SOA parameterization used for cyclic alkane IVOCs. We recommend that future work focus on

481   more detailed speciation of cyclic alkane IVOCs in combustion emissions as well as on chamber and OFR experiments on

482   those speciated compounds to improve quantification of their SOA mass yields.

483

484   As there were no direct measurements of any SOA precursors in the study of Jathar et al. (2017a), we have used previously

485   published emissions profiles for diesel exhaust to determine initial concentrations of the SOA precursors. We examined the

486   sensitivity of model predictions to two different emissions profiles from the EPA SPECIATE (version 4.3) database: Profile

487   #3161 (included in the base case) and Profile #8774 that represents emissions from 'Heavy Duty Diesel Exhaust'; the

488   speciation for both profiles is provided in Tables S1 and S2. Both profiles only included speciation for VOC emissions and in

489   these simulations we assumed an IVOC mass fraction of 60%. The results captured in Figure 5(b) for one of the Idle-Diesel-

490   None experiments show that the choice in the emissions profile had very little influence on the OA evolution, which was

491   expected given that most of the SOA was formed from IVOC, rather than VOC, oxidation. This further demonstrates that

492   IVOCs, not VOCs, play an important role in controlling the SOA formation from diesel exhaust emissions and it is important

493   that future studies work towards better understanding the IVOC speciation.

494

495   The IVOC speciation of Zhao et al. (2015) included 37 unique species, each of which required a unique surrogate to model the

496   SOA formation from that species. Tracking these many IVOC species in an atmospheric model (e.g., global climate model)

497   may be intractable and hence, there is a need to develop simplified parameterizations to efficiently model SOA formation from

498   IVOCs. We note that species using the same surrogate in the VBS model (e.g., a C_{15} linear alkane, C_{17} branched alkane, and

499   C_{13} cyclic alkane are all parameterized using n-pentadecane) could be lumped together to reduce the number of precursors and

500   products tracked and that there are no penalties for a precursor type (e.g., n-alkanes) to include additional precursor and

501   product species once a SOM grid is setup. Nonetheless, to investigate the possibility of developing a simplified

502   parameterization, we modeled SOA from IVOCs assuming that all the IVOCs could be modeled together as a single linear C_{13},

503   C_{15}, or C_{17} alkane; a similar strategy was employed by (Jathar et al., 2014b) to model SOA formation from unspeciated organic

504   compounds in combustion emissions. Results from these simulations are shown in Figure 5(c) for one of the Idle-Diesel-None

505   experiments. For the VBS model, the use of a linear C_{15} and C_{17} alkane parameterization for IVOCs reproduced the

506   measurements well. For the SOM, the use of a linear C_{17} alkane parameterization produced good agreement with

507   measurements. Differences in the VBS and SOM predictions with different alkane parameterizations point to inherent

508   differences in the coupled representation of multigenerational aging and gas/particle partitioning. Results from these

509   simulations indicate that in cases where computational efficiency is demanded, the SOA formation from IVOCs in diesel

510   exhaust could be modeled using a surrogate linear alkane, possibly a C_{15} or a C_{17} linear alkane.

511

512   **3.4 Elemental Composition**

513   The SOM tracks both the carbon and oxygen number of the oxidation products, which allowed us to predict the O:C ratio of

514 the OA. The O:C of the OA was calculated by combining the measured O:C of the POA with the modeled O:C of the SOA. We

515 compare predictions of the O:C of OA from the SOM against measurements for all the experiments listed in Table 1 and at all

516 photochemical exposures in Figure 4; statistical metrics of fractional bias, fractional error, and R^2 for the comparison are listed

517 in Table S5. Model predictions for the no IVOC case, where the O:C of the OA was dominated by the O:C of the aromatic

518 SOA, compared well with measurements (fractional bias = -3%, fractional error = 29%, and R^2 = 0.80). However, the poor OA

519 mass predictions with no IVOCs suggests that the good O:C performance was purely coincidental. Both the 13.76% and 60%

520 IVOC cases under-predicted the OA O:C, on average, by about a factor of two although the 13.76% IVOC case offered a

521 slightly better model performance than the 60% IVOC case (fractional bias = -41%, fractional error = 43%, and R^2 = 0.75 for

522 the 13.76% IVOC case versus fractional bias = -55%, fractional error = 57%, and R^2 = 0.49 for the 60% IVOC case). For both

523 the 13.76% and 60% IVOC cases, the model skill in predicting the O:C was much better for the non-DPF+DOC experiments

524 (R^2 = 0.83 and 0.50 respectively) than for the DPF+DOC experiments (R^2 = 0.02 and 0.29 respectively). Measurements and

525 model predictions of the OA O:C ratio from the 0% and 60% IVOC case as a function of photochemical age are presented in

526 Figure S2.

527

528 The under-prediction in O:C ratios was confounding when compared to earlier applications of the SOM and in light of the

529 reasonable model-measurement comparison found in this work in predicting OA mass. We note that the low O:C in the 13.76%

530 and 60% IVOC cases stems from the dominance of product species that have high carbon numbers and low oxygen numbers.

531 We explored several lines of reasoning for this under-prediction. First, Cappa et al. (2013) found good agreement between the

532 SOM-predicted and observed O:C for chamber experiments conducted using individual linear, branched and cyclic C_{12} alkanes.

533 Also, general predictions of the dependence of O:C on the carbon number of the parent hydrocarbon (cf. Fig. 2b in Cappa and

534 Wilson (2012)) show good agreement with observations (cf. Fig. 2a in Tkacic et al. (2012)), both in terms of absolute values

535 and shape. This suggests that uncertainties in the SOM parameters may not be the dominant reason for the under-prediction. A

536 possible reason for the under-prediction then is that the compounds identified by Zhao et al. (2015) as IVOCs are structurally

537 different than the alkanes used to model them in this work. Second, it is possible that we incorrectly assumed, based on the

538 measured VOC:NO$_x$ ratio (1.9 and 4.1 ppbC ppbN^{-1} for the Idle experiments and 0.06−0.55 ppbC ppbN^{-1} for the Load

539 experiments), that the SOA was formed under high NO$_x$ conditions and that we would need to use SOM parameters developed

540 from high NO$_x$ experiments. In an OFR, high oxidant loadings (OH and O$_3$) could rapidly reduce NO$_x$ at the OFR inlet and

541 result in most of the SOA being formed at low NO$_x$ conditions (Peng and Jimenez, 2017). We performed simulations to

542 examine the sensitivity of model predictions to the use of SOM parameters developed from low NO$_x$ experiments. We found

543 that the SOM resulted in an average increase of only 5% in O:C predictions but an average increase of 65% in OA mass across

544 all experiments at the highest photochemical exposure. A better understanding of the NO$_x$ chemistry inside the OFR (Peng and

545 Jimenez, 2017) might provide insight on the parameterizations needed to model SOA formation in OFRs. Third, the gas-phase

546 chemistry in the OFR might be inherently different than that in a chamber. For example, kinetic limitations to gas/particle

547 partitioning may result in gas-phase oxidation of low-volatility products having high O:C that typically would have partitioned

548 to the particle phase in a chamber experiment but instead are fragmented (Palm et al., 2016). As to why the chamber-based

549 SOM parameters then offer good model performance on OA mass remains unclear. One way in which this issue could be

550 addressed in the future is by developing SOM parameters exclusively based on OFR data, as and when they become available.

551 And finally, the SOM used here did not include surface/heterogeneous and particle-phase reactions that might influence the OA

552 composition and O:C ratio. When heterogeneous reactions of OA were included assuming an OH uptake coefficient of 1 (the

553 product distribution from the oxidation reaction was kept the same as the gas-phase reactions), SOA production at the highest

554   photochemical exposure for all the experiments was reduced, on average, by 10% from fragmentation reactions within the

555   particle phase, but the O:C ratio was only marginally increased (average of 1%).

556

557   To understand the O:C under-prediction better, we compared model predictions of normalized gas-phase species

558   concentrations from the SOM to normalized gas-phase measurements made by Friedman et al. (2017) using a chemical

559   ionization mass spectrometer (CIMS). The CIMS detects an array of oxygenated organic species and the high resolution of the

560   time-of-flight mass spectrometer enables identification of the elemental composition of each detected peak. The CIMS data

561   were aggregated by carbon and oxygen number to facilitate comparison with the SOM data. The comparison was performed on

562   a normalized basis because the CIMS did not provide absolute concentrations for every detected peak. The SOM-CIMS

563   comparisons for the Idle-Diesel-None and Load-Diesel-None experiments at the highest photochemical exposure are shown in

564   Figure 6, which highlight four findings of note. First, the CIMS measured species larger than a carbon number of 12 that are

565   presumably products from oxidation of higher molecular weight organic compounds, although the possibility of dimer

566   formation in the instrument cannot be entirely ruled out. Nonetheless, this provides additional evidence for the presence of

567   IVOC oxidation products in diesel exhaust emissions. Second, the CIMS measured organic compounds with high O:C ratios

568   (e.g., C_6O_6, C_7O_7). This implies that the reaction chemistry in OFRs rapidly adds functional groups to the carbon backbone,

569   although larger, less oxidized compounds could be simultaneously functionalized and fragmented in the CIMS to lead to the

570   appearance of highly oxidized species having only 6 carbon atoms. Third, the SOM offered a reasonable correlation against the

571   CIMS measurements for both experiments across a majority of the carbon-oxygen combinations that spanned more than four

572   orders of magnitude. Qualitatively, this finding validates the statistical evolution of organic compounds tracked through the

573   generalized SOM mechanism, although certainly some differences are evident. Finally, compared to the Idle-Diesel-None

574   experiment, the SOM over-predicted the fractional contribution of low-oxygen number species (O_0 to O_3, factor of 5) and

575   under-predicted some of the high oxygen number species (O_5 to O_7, factor of 2) in the Load-Diesel-None experiment. This

576   under-prediction of the high oxygen number species might potentially explain why the SOM may be under-predicting the OA

577   O:C ratio. The SOM-CIMS comparison is preliminary and we intend to explore the implications of this comparison in future

578   work.

579

580   **3.5 Other Model Sensitivities**

581   We performed sensitivity analyses to examine the influence of other key processes on predictions from both the VBS and SOM

582   models. When examining the sensitivity to each process, all the other inputs were kept the same as those listed in the base case.

583   We only present sensitivity results for the Idle-Diesel-None experiment performed on June 5, as the results for this experiment

584   were generally representative of all experiments (Figure 7). For completeness, we performed simulations for all the

585   experiments at the highest photochemical exposure since each of the processes explored below manifested the strongest

586   response at the highest photochemical exposure. The results from these simulations are presented as a change in the model

587   predictions relative to that offered by the base case.

588

589   *Multi-generational Aging.* One of the key differences between the VBS and the SOM models is how they represent the multi-

590   generational aging of gas-phase products. SOA parameters for the VBS model represent stable product distributions at the end

591   of the chamber experiments and therefore already include the influence of multi-generational aging reactions encountered

592   during the chamber experiment. Additional multi-generational aging in the VBS model, based on the scheme of Robinson et al.

593   (2007), is simulated as a continuous decrease in product volatility, which does not account for fragmentation reactions and has

594   not been constrained against experiments. The SOM framework explicitly models multi-generational aging that includes

595   treatment of fragmentation reactions and constrains the aging reactions based on the chamber experiments to an extent that is

596   determined by the length (in OH exposure space) of the experiment. To test the influence of multi-generational aging, we

597   performed model simulations with aging turned off for the VBS and SOM models and plot the results in Figure 7(a). We found

598   that aging had no influence on model predictions from the VBS model, most likely because the high SOA and OA mass

599   concentrations resulted in a substantial fraction of the organic species to be partitioned to the particle phase. This left very little

600   of the organic species in the gas-phase to participate in multi-generational aging; we calculated that less than 1% by mass of

601   the product species in this experiment was in the gas-phase at the OA mass concentration at the highest photochemical

602   exposure, implying that the SOA mass yields at these OA mass concentrations approached 100% In contrast, the absence of

603   aging resulted in a 46% decrease in the OA mass for the SOM. The decrease was mainly because the first generation oxidation

604   product with the highest yield (i.e., C_xO_1) was too volatile to partition to the particle phase and needed to be aged further to

605   form condensable products. As noted earlier, the term aging is defined differently for the VBS and SOM models and the results

606   presented here need to take the definitional issues into account when examining the influence of aging. Compared to the base

607   case, no aging resulted in an average decrease of <1% and 27% in OA mass for the VBS and SOM models respectively for all

608   experiments at the highest photochemical exposure. These simulations suggest that aging of the oxidation products, at least for

609   the SOM, is as important as the contribution of first generation products to SOA formation.

610

611   *Vapor Wall Losses.* Prior work has highlighted the influence vapor wall losses exert on the calculation of SOA mass yields

612   from chamber experiments (Zhang et al., 2014;Krechmer et al., 2016). Cappa et al. (2016), based on the chamber work of

613   Zhang et al. (2014), recently published parameter sets for the SOM that accounted for no vapor wall losses and two different

614   vapor wall loss rates (1×10^{-4} and 2.5×10^{-4} s^{-1}) assuming an equivalent OA mass of the chamber walls of 10 mg m^{-3} (the base

615   case used the parameter sets for a vapor wall loss rate of 2.5×10^{-4} s^{-1}). We performed model simulations with SOM using

616   parameters that were either not corrected for vapor wall losses or that were corrected for vapor wall losses using either the low

617   (1×10^{-4}) or high (2.5×10^{-4}) estimates proposed by Cappa et al. (2016). The results plotted in Figure 7(b) show that correcting

618   for vapor wall losses slightly increased model predicted OA mass (by 8% and 27% for the low and high cases respectively at

619   the highest photochemical exposure) and provided the best performance for the high estimate for vapor wall losses. Across all

620   experiments and at the highest photochemical exposure, accounting for vapor wall losses using the high estimate resulted in an

621   average increase of 36% over no accounting for vapor wall losses. These comparisons suggest that it is important to use SOA

622   parameterizations in which vapor wall losses in chambers have been accounted for when interpreting SOA experiments.

623   Furthermore, we also simulated the influence of vapor losses to the OFR walls on model predictions. We assumed reversible

624   uptake of vapors to the walls and used a vapor wall loss rate of 2.5×10^{-3} s^{-1} (factor of ~10 larger than that for a chamber) based

625   on the work of Palm et al. (2016) and an equivalent OA mass concentration of 10 mg m^{-3} for the OFR walls. The results plotted

626   in Figure 7(b) show that the loss of vapors to the OFR walls had a small influence on model predictions: a 9% decrease for this

627   experiment and an average decrease of 12% across all experiments at the highest photochemical exposure. Increasing the

628   equivalent OA mass concentration for the OFR walls to 100 and 1000 mg m^{-3} seemed to have no influence on model

629   predictions. These findings imply that vapor wall losses in the presence of sufficient seed aerosol might not be of concern for

630   OFRs (Lambe et al., 2015).

631

632   *Residence Time Distributions.* Model simulations performed in this work assumed that the OFR operated as a plug flow

633   reactor with a constant residence time. Experimental studies by Lambe et al. (2011) and fluid dynamics simulations by Ortega

634   et al. (2016) have shown that OFRs, particularly like the one used in this work, exhibit heterogeneity in residence times. We

635   performed simulations to explore the sensitivity of varying residence times on model predictions. These simulations were

636   performed based on a discretized version of the residence time distribution measured by Lambe et al. (2011) for SO_2 that

637   yielded an average residence time of 100 seconds (same as that used by Jathar et al. (2017a)). The discretized version included

638   six parcels with volume fractions of 0.23, 0.36, 0.24, 0.11, 0.05, and 0.01 with residence times of 45, 65, 100, 200, 300, and

639   500 seconds respectively. Each parcel experienced the same OH concentration but the varying residence times resulted in

640   different OH exposures for each parcel. The parcels were combined after photochemical exposure without repartitioning the

641   OA between the six parcels. Similar to the findings of Peng et al. (2015) for calculating OH exposure, our results in Figure 7(c)

642   show that using a residence time distribution had very little influence on the OA mass evolution compared to use of an

643   effective average time. Compared to the base case, the residence time distribution resulted in an average decrease of 3% and

644   7% in OA mass for the VBS and SOM models respectively for all experiments at the highest photochemical exposure.

645

646   ***Spatial Heterogeneity in OH.*** In addition to the influence exerted by a distribution of residence times, spatial heterogeneity in

647   the gas-phase chemistry inside the OFR (e.g., from radial variation in light intensity) could lead to spatial heterogeneity in OH

648   concentrations and result in a distribution of OH exposures for the sample being aged. We performed simulations to explore the

649   sensitivity of a varying OH exposure on model predictions. These simulations were performed where we split the sample

650   coming into the OFR into two parcels and treated the parcels to different OH exposures. Each experiment was repeated for all

651   combinations (six total) of three different parcel splits (¼-¾, ⅓-⅔, ½-½) and two different OH exposure splits (⅓-X, ⅔-X); X

652   was determined by conserving the total OH exposure reported by Jathar et al. (2017a). For instance, the first simulation was

653   performed by splitting the OFR air parcel into ¼ and ¾ fractions by volume and exposing the ¼ volume to ⅓ the OH exposure.

654   The parcels were combined after photochemical exposure without repartitioning the OA between the two parcels. The results in

655   Figure 7(d) show that the simulated spatial heterogeneity always reduced the OA mass although the maximum reduction (12%

656   for the VBS and 15% for the SOM models) at the highest photochemical exposure was well within the measurement

657   uncertainty. Compared to the base case, the spatial heterogeneity in OH resulted in a maximum decrease of 12% and 14% in

658   OA mass for the VBS and SOM models respectively for all experiments at the highest photochemical exposure.

659

660   **4. Summary and Discussion**

661   Recently, Jathar et al. (2017a) reported on experiments performed using the oxidation flow reactor (OFR) to measure the

662   photochemical production of secondary organic aerosol (SOA) from diesel exhaust under varying engine loads, fuel types, and

663   emissions control systems. These data present an opportunity to not only test SOA models but also use these models to

664   interpret OFR data and determine their relevance for the real atmosphere. In this work, we applied two different SOA model

665   frameworks (VBS and SOM) to simulate the photochemical production of SOA in an OFR from diesel exhaust and evaluated

666   those model frameworks using the data from Jathar et al. (2017a). The volatility basis set (VBS) model is a parameterized

667   model that allows for a volatility-based representation of OA while the statistical oxidation model (SOM) is a semi-explicit

668   parameterized model that uses a carbon-oxygen grid to track OA. Both simulated the coupled chemistry, thermodynamic

669   properties, and gas/particle partitioning of OA and accounted for: (i) semi-volatile and reactive emissions of primary organic

670   aerosol (POA), (ii) SOA production from IVOCs and VOCs, (iii) multi-generational aging, and (iv) kinetic gas/particle

671   partitioning.

672

673   Model predictions suggest that the instantaneous gas/particle partitioning assumption may over-predict SOA formation in

674 OFRs when the initial condensational sinks are low and the condensation of SOA is likely kinetically limited. Hence, SOA

675 formation in OFRs needs to be modeled/interpreted through an explicit treatment of kinetic gas/particle partitioning.

676 Differences in model predictions between instantaneous and kinetic partitioning will depend on the rate at which condensable

677 SOA mass is produced in the OFR (depends on the initial precursor concentrations and photochemical exposure), residence

678 time in the OFR, properties of the condensing species (e.g., diffusion coefficient, molecular weight), and parameters relevant

679 for partitioning (e.g., accommodation coefficient, seed aerosol surface area). To explore the relative importance of

680 instantaneous and kinetically-limited partitioning in an OFR, we used the SOM to simulate SOA formation from diluted diesel

681 exhaust using instantaneous and kinetic partitioning assumptions for varying amounts of SOA formed (0.1-1000 µg m^{-3}) and

682 initial condensational sinks (0.001-10 min^{-1}). The calculations were performed for two different particle sizes (10 and 100 nm)

683 since the condensation of SOA mass would grow the initial condensational sink for the two particles at different rates, i.e. for

684 the same starting initial condensational sink, smaller particles would experience quicker growth in the condensational sink

685 compared to larger particles for the same amount of condensing mass. We assumed a residence time in the OFR of 100 s and

686 an accommodation coefficient of 0.1. The results plotted in Figure 8 show the ratio of SOA predicted through kinetic

687 partitioning to that predicted through instantaneous partitioning as a function of the initial condensational sink and the SOA

688 formed under an instantaneous partitioning assumption. We found that the SOA formation in the OFR was kinetically-limited

689 over most of input ranges explored and approached the SOA formed under the instantaneous partitioning assumption either

690 when the initial condensational sink was very large (>5 min^{-1}) or when a large amount of condensable SOA was produced in

691 the OFR (>=1000 µg m^{-3} for the 10 nm particles and >>10000 µg m^{-3} for the 100 nm particles). Our finding implies that

692 ambient applications of the OFR, where initial condensational sinks are typically smaller (~0.005-0.5 min^{-1}) and the maximum

693 SOA produced is typically less than 20 µg m^{-3}, will only produce a small fraction (1-30%) of the intended SOA. Although

694 these simulation results need to be verified experimentally, they do suggest that it might be challenging to operate the OFR in

695 conditions where instantaneous or atmospherically-relevant partitioning is applicable, further complicating the coupled

696 atmospheric simulation of chemistry and thermodynamics in OFRs.

697

698 Upon including IVOCs as SOA precursors, both the VBS and SOM models were able to reasonably predict the OA mass

699 evolution reported by Jathar et al. (2017a) across different engine loads, fuel types, and emissions control systems. Model

700 predictions suggest that 40% of the unburned hydrocarbon emissions are likely IVOCs and that these IVOCs (regardless of the

701 emissions profiles used to determine non-IVOC emissions) would account for most (>90%) of the SOA formed from diesel

702 exhaust. These findings are consistent with prior work from chamber experiments (Jathar et al., 2014b) and modeling studies

703 (Zhao et al., 2015). Simulations performed using single surrogates suggest that the complex mixture of IVOCs in diesel

704 exhaust could be well represented using a linear C_{15} or C_{17} alkane. These offer a computationally-efficient strategy to model

705 SOA formation from IVOCs in large-scale three-dimensional models. The SOM tracks the carbon and oxygen numbers of the

706 oxidation products and hence model predictions were used to calculate atomic O:C ratios for OA, which were then compared to

707 measurements. While the inclusion of IVOCs allowed for good model-measurement comparisons on OA mass, the SOM

708 under-predicted the O:C ratio of OA by a factor of two, possibly highlighting the limitations in modeling the IVOCs as alkanes

709 and/or extrapolating chamber-based parameterizations to OFR experiments. Model predictions of the gas-phase organic species

710 compared favorably to those measured using a chemical ionization mass spectrometer (CIMS), which qualitatively validates

711 the statistical evolution of organic compounds tracked through the generalized SOM mechanism.

712

713 As OFRs are increasingly used to study SOA formation and evolution in laboratory and field environments, there is a need to

714   develop models that can be used to interpret OFR data. This work suggests that multi-generational aging (in case of the VBS

715   model), residence time distributions, and spatial heterogeneity in OH concentrations produced sensitivities that were well

716   within the measurement uncertainty and were not a concern for the model system studied. However, model predictions did

717   appear to be more sensitive to multi-generational aging (in case of the SOM) and influence of vapor wall losses, highlighting

718   that these processes be included in OFR models. While the conclusions from this work may be relevant for other laboratory

719   and ambient studies, their relative importance may vary. There are several instances where the model development was

720   insufficient and will likely be addressed in future work. For example, the model could benefit from the use of a polydisperse

721   size distribution to treat new particle formation and growth and improve predictions of the evolution of the aerosol size

722   distribution. Similarly, the model needs to be rigorously tested against other laboratory (e.g., Lambe et al. (2012)) and ambient

723   (e.g., Palm et al. (2016)) OFR data.

724

725   **5 Acknowledgements**

726   We thank the Dr. Jeffrey Pierce and Dr. John Volckens for their feedback on the written manuscript. DKF acknowledges the

727   Beckman Young Investigator Award for funding.

728

729   **6 References**

730   Ahmadov, R., McKeen, S. A., Robinson, A. L., Bahreini, R., Middlebrook, A. M., de Gouw, J. A., Meagher, J., Hsie,

731   E. Y., Edgerton, E., Shaw, S., and Trainer, M.: A volatility basis set model for summertime secondary organic aerosols over

732   the eastern United States in 2006, Journal Of Geophysical Research-Atmospheres, 117, D06301, 2012.

733   Anderson, J. O., Thundiyil, J. G., and Stolbach, A.: Clearing the air: a review of the effects of particulate matter air

734   pollution on human health, Journal of Medical Toxicology, 8, 166-175, 2012.

735   Atkinson, R., and Arey, J.: Atmospheric degradation of volatile organic compounds, Chemical Reviews, 103, 4605-

736   4638, 2003.

737   Bond, T., Venkataraman, C., and Masera, O.: Global atmospheric impacts of residential fuels, Energy for Sustainable

738   Development, 8, 20-32, 2004.

739   Cappa, C., and Wilson, K.: Multi-generation gas-phase oxidation, equilibrium partitioning, and the formation and

740   evolution of secondary organic aerosol, Atmospheric Chemistry and Physics, 12, 9505-9528, 2012.

741   Cappa, C. D., Zhang, X., Loza, C. L., Craven, J. S., Yee, L. D., and Seinfeld, J. H.: Application of the Statistical

742   Oxidation Model (SOM) to Secondary Organic Aerosol formation from photooxidation of C 12 alkanes, Atmospheric

743   Chemistry and Physics, 13, 1591-1606, 2013.

744   Cappa, C. D., Jathar, S. H., Wexler, A. S., Seinfeld, J., and Kleeman, M. J.: Simulating secondary organic aerosol in a

745   regional air quality model using the statistical oxidation model – Part 2: Assessing the influence of vapor wall losses,

746   Atmospheric Chemistry & Physics, 16, 3041-3059, 2016.

747   Chacon-Madrid, H., and Donahue, N.: Fragmentation vs. functionalization: chemical aging and organic aerosol

748   formation, Atmos. Chem. Phys, 11, 10553-10563, doi:10.5194/acp-11-10553-2011 2011.

749   Chen, S., Brune, W., Lambe, A., Davidovits, P., and Onasch, T.: Modeling organic aerosol from the oxidation of

750   alpha-pinene in a Potential Aerosol Mass (PAM) chamber, Atmospheric Chemistry and Physics, 13, 5017-5031, 2013.

751   Chirico, R., DeCarlo, P., Heringa, M., Tritscher, T., Richter, R., Prevot, A., Dommen, J., Weingartner, E., and Wehrle,

752   G.: Impact of aftertreatment devices on primary emissions and secondary organic aerosol formation potential from in-use

753   diesel vehicles: results from smog chamber experiments, Atmospheric Chemistry and Physics, 10, 11545-11563, 2010.

754   Donahue, N., Robinson, A., Stanier, C., and Pandis, S.: Coupled partitioning, dilution, and chemical aging of

755 semivolatile organics, Environ. Sci. Technol, 40, 2635-2643, doi:10.1021/es052297c, 2006a.

756   Donahue, N., Epstein, S., Pandis, S., and Robinson, A.: A two-dimensional volatility basis set: 1. organic-aerosol

757 mixing thermodynamics, Atmospheric Chemistry and Physics, 11, 3303-3318, 2011.

758   Donahue, N. M., Robinson, A. L., Stanier, C. O., and Pandis, S. N.: Coupled partitioning, dilution, and chemical aging

759 of semivolatile organics., Environ. Sci. Technol., 40, 2635-2643, 2006b.

760   Dzepina, K., Volkamer, R., Madronich, S., Tulet, P., Ulbrich, I., Zhang, Q., Cappa, C., Ziemann, P., and Jimenez, J.:

761 Evaluation of recently-proposed secondary organic aerosol models for a case study in Mexico City, Atmospheric Chemistry

762 and Physics, 9, 5681-5709, doi:10.5194/acp-9-5681-2009, 2009.

763   Ensberg, J. J., Hayes, P. L., Jimenez, J. L., Gilman, J. B., Kuster, W. C., de Gouw, J. A., Holloway, J. S., Gordon, T.

764 D., Jathar, S., and Robinson, A. L.: Emission factor ratios, SOA mass yields, and the impact of vehicular emissions on SOA

765 formation, Atmospheric Chemistry and Physics, 14, 2383-2397, 2014.

766   EPA: SPECIATE Version 4.3, in, 2013.

767   EPA: Estimation Programs Interface Suite™. , in, United States Environmental Protection Agency, Washington, DC,

768 USA., 2017.

769   Friedman, B., Brophy, P., Brune, W. H., and Farmer, D. K.: Anthropogenic Sulfur Perturbations on Biogenic

770 Oxidation: SO2 Additions Impact Gas-Phase OH Oxidation Products of α- and β-Pinene, Environ. Sci. Technol., 50, 1269-

771 1279, 10.1021/acs.est.5b05010, 2016.

772   Friedman, B., Link, M. F., Fulgham, S. R., Brophy, P., Galang, A., Brune, W. H., Jathar, S. H., and Farmer, D. K.:

773 Primary and Secondary Sources of Gas-Phase Organic Acids from Diesel Exhaust, Environ. Sci. Technol., 51, 10872-10880,

774 10.1021/acs.est.7b01169, 2017.

775   Fuzzi, S., Baltensperger, U., Carslaw, K., Decesari, S., Denier van der Gon, H., Facchini, M. C., Fowler, D., Koren, I.,

776 Langford, B., Lohmann, U., Nemitz, E., Pandis, S., Riipinen, I., Rudich, Y., Schaap, M., Slowik, J. G., Spracklen, D. V.,

777 Vignati, E., Wild, M., Williams, M., and Gilardoni, S.: Particulate matter, air quality and climate: lessons learned and future

778 needs, Atmos. Chem. Phys., 15, 8217-8299, 10.5194/acp-15-8217-2015, 2015.

779   Gentner, D. R., Jathar, S. H., Gordon, T. D., Bahreini, R., Day, D. A., El Haddad, I., Hayes, P. L., Pieber, S. M., Platt,

780 S. M., and de Gouw, J. A.: A review of urban secondary organic aerosol formation from gasoline and diesel motor vehicle

781 emissions, Environ. Sci. Technol., 2016.

782   Gordon, T. D., Nguyen, N. T., Presto, A. A., Lipsky, E. M., Maldonado, S., Maricq, M., and Robinson, A. L.:

783 Secondary organic aerosol production from diesel vehicle exhaust: impact of aftertreatment, fuel chemistry and driving cycle,

784 Atmospheric Chemistry & Physics, 14, 4643-4659, doi:10.5194/acp-14-4643-2014, 2014.

785   Hayes, P., Carlton, A., Baker, K., Ahmadov, R., Washenfelder, R., Alvarez, S., Rappenglück, B., Gilman, J., Kuster,

786 W., and de Gouw, J.: Modeling the formation and aging of secondary organic aerosols in Los Angeles during CalNex 2010,

787 Atmospheric Chemistry and Physics, 15, 5773-5801, 2015.

788   Hodzic, A., Jimenez, J., Madronich, S., Canagaratna, M., DeCarlo, P., Kleinman, L., and Fast, J.: Modeling organic

789 aerosols in a megacity: potential contribution of semi-volatile and intermediate volatility primary organic compounds to

790 secondary organic aerosol formation, Atmospheric Chemistry and Physics, 10, 5491-5514, doi:10.5194/acp-10-5491-2010,

791 2010.

792   Huffman, J., Docherty, K., Mohr, C., Cubison, M., Ulbrich, I., Ziemann, P., Onasch, T., and Jimenez, J.: Chemically-

793 resolved volatility measurements of organic aerosol from different sources, Environ. Sci. Technol., 43, 5351-5357, 2009.

794   Jathar, S., Farina, S., Robinson, A., and Adams, P.: The influence of semi-volatile and reactive primary emissions on

795   the abundance and properties of global organic aerosol, Atmospheric Chemistry and Physics, 11, 7727-7746, doi:10.5194/acp-

796   11-7727-2011 2011.

797   Jathar, S. H., Donahue, N. M., Adams, P. J., and Robinson, A. L.: Testing secondary organic aerosol models using

798   smog chamber data for complex precursor mixtures: influence of precursor volatility and molecular structure, Atmospheric

799   Chemistry and Physics, 14, 5771-5780, 2014a.

800   Jathar, S. H., Gordon, T. D., Hennigan, C. J., Pye, H. O. T., Pouliot, G. A., Adams, P. J., Donahue, N. M., and

801   Robinson, A. L.: Unspeciated organic emissions from combustion sources and their influence on the secondary organic aerosol

802   budget in the United States, Proceedings of the National Academy of Sciences, 111, 10473-10478, 2014b.

803   Jathar, S. H., Cappa, C. D., Wexler, A. S., Seinfeld, J. H., and Kleeman, M. J.: Multi-generational oxidation model to

804   simulate secondary organic aerosol in a 3-D air quality model, Geosci. Model Dev., 8, 2553-2567, 10.5194/gmd-8-2553-2015,

805   2015.

806   Jathar, S. H., Cappa, C. D., Wexler, A. S., Seinfeld, J. H., and Kleeman, M. J.: Simulating secondary organic aerosol

807   in a regional air quality model using the statistical oxidation model – Part 1: Assessing the influence of constrained multi-

808   generational ageing, Atmospheric Chemistry & Physics, 16, 2309-2322, 2016.

809   Jathar, S. H., Friedman, B., Galang, A. A., Link, M. F., Brophy, P., Volckens, J., Eluri, S., and Farmer, D. K.: Linking

810   Load, Fuel and Emission Controls to Photochemical Production of Secondary Organic Aerosol from a Diesel Engine, Environ.

811   Sci. Technol., 2017a.

812   Jathar, S. H., Woody, M., Pye, H. O., Baker, K. R., and Robinson, A. L.: Chemical transport model simulations of

813   organic aerosol in southern California: model evaluation and gasoline and diesel source contributions, Atmospheric Chemistry

814   and Physics, 17, 4305-4318, 2017b.

815   Karnezi, E., Riipinen, I., and Pandis, S.: Measuring the atmospheric organic aerosol volatility distribution: a

816   theoretical analysis, Atmospheric Measurement Techniques, 7, 2953-2965, 2014.

817   Konovalov, I. B., Beekmann, M., Berezin, E. V., Petetin, H., Mielonen, T., Kuznetsova, I. N., and Andreae, M. O.:

818   The role of semi-volatile organic compounds in the mesoscale evolution of biomass burning aerosol: a modelling case study of

819   the 2010 mega-fire event in Russia, Atmospheric Chemistry and Physics Discussions, 15, 9107-9172, 2015.

820   Krechmer, J. E., Pagonis, D., Ziemann, P. J., and Jimenez, J. L. L.: Quantification of gas-wall partitioning in Teflon

821   environmental chambers using rapid bursts of low-volatility oxidized species generated in-situ, Environ. Sci. Technol., 2016.

822   Kroll, J. H., Smith, J. D., Che, D. L., Kessler, S. H., Worsnop, D. R., and Wilson, K. R.: Measurement of

823   fragmentation and functionalization pathways in the heterogeneous oxidation of oxidized organic aerosol, Physical Chemistry

824   Chemical Physics, 11, 8005-8014, 2009.

825   Lambe, A., Chhabra, P., Onasch, T., Brune, W., Hunter, J., Kroll, J., Cummings, M., Brogan, J., Parmar, Y., and

826   Worsnop, D.: Effect of oxidant concentration, exposure time, and seed particles on secondary organic aerosol chemical

827   composition and yield, Atmospheric Chemistry and Physics, 15, 3063-3075, 2015.

828   Lambe, A. T., Ahern, A. T., Williams, L. R., Slowik, J. G., Wong, J. P. S., Abbatt, J. P. D., Brune, W. H., Ng, N. L.,

829   Wright, J. P., and Croasdale, D. R.: Characterization of aerosol photooxidation flow reactors: heterogeneous oxidation,

830   secondary organic aerosol formation and cloud condensation nuclei activity measurements, Atmospheric Measurement

831   Techniques, 4, 445-461, 2011.

832   Lambe, A. T., Onasch, T. B., Croasdale, D. R., Wright, J. P., Martin, A. T., Franklin, J. P., Massoli, P., Kroll, J. H.,

833   Canagaratna, M. R., and Brune, W. H.: Transitions from functionalization to fragmentation reactions of laboratory secondary

834   organic aerosol (SOA) generated from the OH oxidation of alkane precursors, Environ. Sci. Technol., 46, 5430-5437, 2012.

835   Lee, B.-H., Pierce, J. R., Engelhart, G. J., and Pandis, S. N.: Volatility of secondary organic aerosol from the

836   ozonolysis of monoterpenes, Atmospheric environment, 45, 2443-2452, 2011.

837   Lim, Y. B., and Ziemann, P. J.: Effects of molecular structure on aerosol yields from OH radical-initiated reactions of

838   linear, branched, and cyclic alkanes in the presence of NO x, Environ. Sci. Technol., 43, 2328-2334, 2009.

839   Link, M., Friedman, B., Fulgham, R., Brophy, P., Galang, A., Jathar, S., Veres, P., Roberts, J., and Farmer, D.:

840   Photochemical processing of diesel fuel emissions as a large secondary source of isocyanic acid (HNCO), Geophysical

841   Research Letters, 43, 4033-4041, 2016.

842   May, A. A., Levin, E. J. T., Hennigan, C. J., Riipinen, I., Lee, T., Collett, J. L., Jimenez, J. L., Kreidenweis, S. M., and

843   Robinson, A. L.: Gas-particle partitioning of primary organic aerosol emissions: 3. Biomass burning, Journal of Geophysical

844   Research: Atmospheres, 118, 2013JD020286, 10.1002/jgrd.50828, 2013a.

845   May, A. A., Presto, A. A., Hennigan, C. J., Nguyen, N. T., Gordon, T. D., and Robinson, A. L.: Gas-particle

846   partitioning of primary organic aerosol emissions: (2) Diesel vehicles, Environ. Sci. Technol., 47, 8288-8296, 2013b.

847   May, A. A., Presto, A. A., Hennigan, C. J., Nguyen, N. T., Gordon, T. D., and Robinson, A. L.: Gas-particle

848   partitioning of primary organic aerosol emissions: (1) gasoline vehicle exhaust, Atmospheric Environment, 77, 128-139,

849   2013c.

850   Murphy, B., and Pandis, S.: Simulating the formation of semivolatile primary and secondary organic aerosol in a

851   regional chemical transport model., Environ. Sci. Technol., 43, 4722-4728, doi:10.1021/es803168a, 2009.

852   Odum, J. R., Hoffmann, T., Bowman, F., Collins, D., Flagan, R. C., and Seinfeld, J. H.: Gas/particle partitioning and

853   secondary organic aerosol yields, Environ. Sci. Technol., 30, 2580-2585, 1996.

854   Ortega, A. M., Hayes, P. L., Peng, Z., Palm, B. B., Hu, W., Day, D. A., Li, R., Cubison, M. J., Brune, W. H., and

855   Graus, M.: Real-time measurements of secondary organic aerosol formation and aging from ambient air in an oxidation flow

856   reactor in the Los Angeles area, Atmospheric Chemistry and Physics, 16, 7411-7433, 2016.

857   Pachauri, R. K., Allen, M. R., Barros, V. R., Broome, J., Cramer, W., Christ, R., Church, J. A., Clarke, L., Dahe, Q.,

858   Dasgupta, P., Dubash, N. K., Edenhofer, O., Elgizouli, I., Field, C. B., Forster, P., Friedlingstein, P., Fuglestvedt, J., Gomez-

859   Echeverri, L., Hallegatte, S., Hegerl, G., Howden, M., Jiang, K., Jimenez Cisneroz, B., Kattsov, V., Lee, H., Mach, K. J.,

860   Marotzke, J., Mastrandrea, M. D., Meyer, L., Minx, J., Mulugetta, Y., O'Brien, K., Oppenheimer, M., Pereira, J. J., Pichs-

861   Madruga, R., Plattner, G. K., Pörtner, H.-O., Power, S. B., Preston, B., Ravindranath, N. H., Reisinger, A., Riahi, K.,

862   Rusticucci, M., Scholes, R., Seyboth, K., Sokona, Y., Stavins, R., Stocker, T. F., Tschakert, P., van Vuuren, D., and van

863   Ypserle, J. P.: Climate Change 2014: Synthesis Report. Contribution of Working Groups I, II and III to the Fifth Assessment

864   Report of the Intergovernmental Panel on Climate Change, edited by: Pachauri, R. K., and Meyer, L., IPCC, Geneva,

865   Switzerland, 151 pp., 2014.

866   Palm, B. B., Campuzano-Jost, P., Ortega, A. M., Day, D. A., Kaser, L., Jud, W., Karl, T., Hansel, A., Hunter, J. F.,

867   and Cross, E. S.: In situ secondary organic aerosol formation from ambient pine forest air using an oxidation flow reactor,

868   Atmospheric Chemistry and Physics, 16, 2943-2970, 2016.

869   Pankow, J. F.: An absorption model of gas/particle partitioning of organic compounds in the atmosphere, Atmospheric

870   Environment, 28, 185-188, 1994.

871   Pankow, J. F., and Barsanti, K. C.: The carbon number-polarity grid: A means to manage the complexity of the mix of

872   organic compounds when modeling atmospheric organic particulate matter, Atmospheric Environment, 43, 2829-2835, 2009.

873   Peng, Z., Day, D., Stark, H., Li, R., Lee-Taylor, J., Palm, B., Brune, W., and Jimenez, J.: HOx radical chemistry in

874 oxidation flow reactors with low-pressure mercury lamps systematically examined by modeling, Atmospheric Measurement
875 Techniques, 8, 4863-4890, 2015.
876 Peng, Z., and Jimenez, J. L.: Modeling of the chemistry in oxidation flow reactors with high initial NO, Atmos. Chem.
877 Phys. Discuss., 2017, 1-37, 10.5194/acp-2017-266, 2017.
878 Presto, A. A., Nguyen, N. T., Ranjan, M., Reeder, A. J., Lipsky, E. M., Hennigan, C. J., Miracolo, M. A., Riemer, D.
879 D., and Robinson, A. L.: Fine particle and organic vapor emissions from staged tests of an in-use aircraft engine, Atmospheric
880 Environment, 45, 3603-3612, 2011.
881 Pye, H., and Seinfeld, J.: A global perspective on aerosol from low-volatility organic compounds, Atmos. Chem.
882 Phys, 10, 4377-4401, doi:10.5194/acp-10-4377-2010, 2010.
883 Robinson, A. L., Donahue, N. M., Shrivastava, M. K., Weitkamp, E. A., Sage, A. M., Grieshop, A. P., Lane, T. E.,
884 Pierce, J. R., and Pandis, S. N.: Rethinking organic aerosols: Semivolatile emissions and photochemical aging, Science, 315,
885 1259-1262, 2007.
886 Saleh, R., Donahue, N. M., and Robinson, A. L.: Time scales for gas-particle partitioning equilibration of secondary
887 organic aerosol formed from alpha-pinene ozonolysis, Environ. Sci. Technol., 47, 5588-5594, 2013.
888 Seinfeld, J. H., and Pandis, S. N.: Atmospheric Chemistry and Physics, John Wiley and Sons., New York, 2006.
889 Simonen, P., Saukko, E., Karjalainen, P., Timonen, H., Bloss, M., Aakko-Saksa, P., Rönkkö, T., Keskinen, J., and Dal
890 Maso, M.: A new oxidation flow reactor for measuring secondary aerosol formation of rapidly changing emission sources,
891 Atmospheric Measurement Techniques, 10, 1519, 2017.
892 Tkacik, D. S., Presto, A. A., Donahue, N. M., and Robinson, A. L.: Secondary organic aerosol formation from
893 intermediate-volatility organic compounds: cyclic, linear, and branched alkanes, Environ. Sci. Technol., 46, 8773-8781, doi:
894 10.1021/es301112c, 2012.
895 Tkacik, D. S., Lambe, A. T., Jathar, S., Li, X., Presto, A. A., Zhao, Y., Blake, D., Meinardi, S., Jayne, J. T., Croteau,
896 P. L., and Robinson, A. L.: Secondary Organic Aerosol Formation from in-Use Motor Vehicle Emissions Using a Potential
897 Aerosol Mass Reactor, Environ. Sci. Technol., 48, 11235-11242, 10.1021/es502239v, 2014.
898 Tsimpidi, A., Karydis, V., Zavala, M., Lei, W., Molina, L., Ulbrich, I., Jimenez, J., and Pandis, S.: Evaluation of the
899 volatility basis-set approach for the simulation of organic aerosol formation in the Mexico City metropolitan area, Atmos.
900 Chem. Phys, 10, 525-546, doi:10.5194/acp-10-525-2010, 2009.
901 Zhang, X., Cappa, C. D., Jathar, S. H., McVay, R. C., Ensberg, J. J., Kleeman, M. J., and Seinfeld, J. H.: Influence of
902 vapor wall loss in laboratory chambers on yields of secondary organic aerosol, Proceedings of the National Academy of
903 Sciences, 111, 5802-5807, 2014.
904 Zhao, Y., Nguyen, N. T., Presto, A. A., Hennigan, C. J., May, A. A., and Robinson, A. L.: Intermediate volatility
905 organic compound emissions from on-road diesel vehicles: chemical composition, emission factors, and estimated secondary
906 organic aerosol production, Environ. Sci. Technol., 49, 11516-11526, 2015.
907

7 Tables

Table 1: Primary emissions of THC and POA, maximum photochemical production of SOA, maximum O:C of the OA, maximum OH exposure, and size distribution data.

Load-Fuel-Aftertreatment Experiment	Date	THC ($\mu g\ m^{-3}$)	POA ($\mu g\ m^{-3}$)	SOA[%] ($\mu g\ m^{-3}$)	O: C[%]	OH[%] (molec.-hr cm^{-3})	Number Mean Dia.[*] (nm)	Number Conc.[*] ([#] cm^{-3})
Idle-Diesel-None	June 3	1519	38±15	209±66	0.23±0.01	2.1×10^7		8.0×10^5
	June 5	1810	35±11	875±288	0.46±0.07	6.67×10^7	46	6.5×10^5
	June 12	2554	85±17	877±277	0.57±0.09	3.61×10^7		3.4×10^5
Idle-Biodiesel-None	June 4	1118	22±12	999±316	0.52±0.07	9.17×10^7	46[@]	$7.3\times10^{5@}$
	June 8	2160	69±20	1415±468	0.36±0.03	4.72×10^7		$4.1\times10^{5@}$
Load-Diesel-None	June 3	959	19±11	181±58	0.37±0.01	3.6×10^7	190	5.3×10^5
	June 5	711	37±13	253±100	0.32±0.04	2.61×10^7		4.4×10^5
Load- Biodiesel-None	June 4	1634	29±18	645±204	0.38±0.05	2.78×10^7	190[@]	$5.0\times10^{5@}$
	June 8	518	46±22	284±106	0.30±0.04	1.42×10^7		$3.3\times10^{5@}$
Idle-Diesel-DPF+DOC	June 9	2135	1.5±0.6	1040±335	0.37±0.02	5×10^7	52	910
Load-Diesel-DPF+DOC	June 9	303	1.6±3.6	146±48	0.29±0.01	1.31×10^7	57	968
Idle-Biodiesel-DPF+DOC	June 10	1773	2.6±1	787±250	0.44±0.04	5.28×10^7	52[@]	910[@]
Load-Biodiesel-DPF+DOC	June 10	261	2±0.14	107±9	0.29±0.01	1.39×10^7	57[@]	968[@]

DPF=diesel particulate filter, DOC=diesel oxidation catalyst
[%]maximum values measured in each experiment
[*]values measured at no OH exposure
[@]No data, assumed to be similar to the equivalent diesel experiment for the model

Table 2: SOA precursors and mass yields used in the VBS model.

Species	$log_{10}C^*$					Reference
	0.1	1	10	100	1000	
toluene	0.0000	0.0100	0.2400	0.4500	0.7000	Hildebrandt et al.,2009
benzene	0.0392	0.0315	0.0000	0.8230	0.0957	Ng et al., 2007[#]
m-xylene	0.0032	0.0106	0.0633	0.0465	0.0000	Ng et al., 2007[#]
p-xylene	0.0000	0.0022	0.0764	0.0000	0.0000	Song et al., 2007[#]
o-xylene	0.0000	0.0132	0.1140	0.0000	0.0000	Song et al., 2007[#]
naphthalene	0.0000	0.1660	0.0000	0.5400	0.8130	Chan et al., 2009[#]
1-methylnaphthalene	0.0000	0.0170	0.4860	0.0000	0.0000	Chan et al., 2009[#]
2-methylnaphthalene	0.0000	0.0531	0.5040	0.0000	0.0000	Chan et al., 2009[#]
1,2-dimethylnaphthalene	0.0000	0.3100	0.0000	0.0000	0.0000	Chan et al., 2009[#]
1-methyl-3-n-propylbenzene	0.0000	0.0000	0.0405	0.0694	0.1140	Odum et al.,1997[#]
n-decane	0.0000	0.0000	0.0110	0.1280	0.2420	Presto et al., 2010[&]
n-undecane	0.0000	0.0040	0.0720	0.1760	0.1450	Presto et al., 2010[&]
n-dodecane	0.0000	0.0140	0.1100	0.1600	0.0000	Presto et al., 2010
n-tridecane	0.0140	0.0590	0.0940	0.0710	0.0000	Presto et al., 2010
n-tetradecane	0.0940	0.3000	0.3500	0.0000	0.0000	Presto et al., 2010
n-pentadecane	0.0440	0.0710	0.4100	0.3000	0.0000	Presto et al., 2010
n-hexadecane	0.0530	0.0830	0.4600	0.2500	0.0000	Presto et al., 2010
n-heptadecane	0.0630	0.0890	0.5500	0.2000	0.0000	Presto et al., 2010
n-octadecane	0.0760	0.3195	0.3750	0.1000	0.0000	Presto et al., 2010[&]
n-nonadecane	0.0890	0.5500	0.2000	0.0000	0.0000	Presto et al., 2010[&]
n-eicosane	0.3195	0.3750	0.1000	0.0000	0.0000	Presto et al., 2010[&]
n-heneicosane	0.5500	0.2000	0.0000	0.0000	0.0000	Presto et al., 2010[&]
n-docosane	0.3750	0.1000	0.0000	0.0000	0.0000	Presto et al., 2010[&]
n- tricosane	0.2000	0.000	0.0000	0.0000	0.0000	Presto et al., 2010[&]

[&]extrapolated from the Presto et al. (2010) data
[#]do not account for vapor wall losses

Table 3: SOA precursors and parameters used in the SOM (Cappa et al., 2016).

Species	m_{frag}	ΔLVP	$p_{O,1}$	$p_{O,2}$	$p_{O,3}$	$p_{O,4}$	Reference
n-dodecane	0.0980	1.3900	0.9270	0.0101	0.0180	0.0445	Loza et al. (2014)
methylundecane	0.0100	1.2100	0.7419	0.0011	0.1820	0.0750	Loza et al. (2014)
hexylcyclohexane	0.0477	1.5700	0.7313	0.0381	0.2101	0.0205	Loza et al. (2014)
toluene	0.2220	1.2400	0.0029	0.0010	0.0010	1.0100	Zhang et al. (2014)
benzene	0.5350	1.7000	0.0792	0.0010	0.9190	0.0010	Ng et al. (2007)
m-xylene	0.0100	1.6800	0.9360	0.0010	0.0021	0.0609	Ng et al. (2007)
naphthalene	0.1210	1.3100	0.6440	0.0010	0.0460	0.3080	Chan et al. (2009)

922
923 *Table 4: (a) Volatility- and (b) carbon-number resolved distributions used to determine mass concentrations of POC in the*
924 *VBS and SOM models respectively. The volatility distributions are from (May et al., 2013b)..*

C^* ($\mu g\ m^{-3}$)	10^{-2}	10^{-1}	10^1	10^2	10^3	10^4	10^5	10^6
f_i	0.03	0.25	0.37	0.23	0.06	0.03	0.01	0.01

925

Carbon No.	<16	16	17	18	19	20	21	22	23	24	25	26	>26
f_i	0.003	0.000	0.058	0.043	0.055	0.094	0.146	0.181	0.178	0.137	0.078	0.026	0.001

926
927 *Table 5: Reaction rate constants (k_{OH}), mass fractions, and VBS and SOM surrogates for SOA precursors in diesel and*
928 *biodiesel emissions. k_{OH} values are from Atkinson and Arey (2003) when available or the EPI Suite version 4.11 (EPA, 2017).*

Species	Carbon Number	k_{OH} (cm^3 molecules^{-1} s^{-1})	Mass Percentage of THC		VBS Surrogate	SOM Surrogate
			Diesel	Biodiesel		
ethylbenzene	8	7.0×10^{-12}	0.144	0.071	toluene	toluene
indan	9	1.9×10^{-11}	0.087	NA	naphthalene	naphthalene
butylbenzene	10	4.5×10^{-12}	0.065	0.405	m-xylene	m-xylene
diethylbenzene	10	8.11×10^{-12}	0.101	NA	m-xylene	m-xylene
isopropyltoluene	10	8.54×10^{-12}	NA	0.308	toluene	toluene
m-xylene	8	2.31×10^{-11}	0.282	0.318	m-xylene	m-xylene
o-xylene	8	1.36×10^{-11}	0.157	0.338	o-xylene	m-xylene
p-xylene	8	1.43×10^{-11}	0.046	NA	p-xylene	m-xylene
n-decane	10	1.1×10^{-11}	0.245	1.460	n-decane	n-decane
n-undecane	11	1.23×10^{-11}	0.120	1.660	n-undecane	n-dodecane
toluene	7	5.63×10^{-12}	1.405	0.680	toluene	toluene
n-tridecane	13	1.68×10^{-11}	NA	0.525	n-tridecane	n-dodecane
benzaldehyde	7	1.2×10^{-11}	0.324	NA	benzene	benzene
benzene	6	1.22×10^{-12}	0.925	1.370	benzene	benzene
C_{10} aromatics	10	2.3×10^{-11}	0.037	NA	m-xylene	m-xylene
C_9 aromatics	9	2.31×10^{-11}	0.230	NA	m-xylene	m-xylene
1,2,3-trimethylbenzene	9	3.27×10^{-11}	0.056	NA	m-xylene	m-xylene
1,2,4-trimethylbenzene	9	3.25×10^{-11}	0.245	0.404	m-xylene	m-xylene
1,2-diethylbenzene	10	8.11×10^{-12}	0.041	NA	toluene	toluene
1,3,5-trimethylbenzene	9	5.67×10^{-11}	NA	0.162	m-xylene	m-xylene
1,2-dimethyl-4-ethylbenzene	10	1.69×10^{-11}	NA	0.176	m-xylene	m-xylene
1,3-dimethyl-2-ethylbenzene	10	1.76×10^{-11}	NA	0.283	m-xylene	m-xylene
1,4-dimethyl-2-ethylbenzene	10	1.69×10^{-11}	NA	0.370	m-xylene	m-xylene
1-(1,1-dimethylethyl)-3,5-dimethylbenzene	12	3.01×10^{-11}	NA	0.318	m-xylene	m-xylene
1-methyl-2-ethylbenzene	9	7.44×10^{-12}	0.065	0.328	toluene	toluene
1-methyl-3-ethylbenzene	9	1.39×10^{-11}	0.116	0.616	toluene	toluene
1-methyl-2-tert-butylbenzene	11	6.74×10^{-12}	NA	0.369	toluene	toluene
1-tert-butyl-4-ethylbenzene	12	7.42×10^{-12}	NA	0.166	m-xylene	m-xylene
2-methyl-butyl-benzene	11	1.02×10^{-11}	NA	0.945	m-xylene	m-xylene
3,3-dimethyloctane	10	7.21×10^{-12}	NA	0.262	n-decane	methylundecane
3-ethyloctane	10	1.18×10^{-11}	NA	0.162	n-decane	methylundecane
3-methylnonane	10	1.14×10^{-11}	NA	0.227	n-decane	methylundecane

C_{12} branched alkane	12	1.82×10^{-11}	2.268	2.268	*n*-decane	methylundecane
C_{13} branched alkane	13	1.68×10^{-11}	1.623	1.623	*n*-undecane	methylundecane
C_{14} branched alkane	14	1.39×10^{-11}	1.052	1.052	*n*-dodecane	methylundecane
C_{15} branched alkane	15	1.82×10^{-11}	0.939	0.939	*n*-tridecane	methylundecane
C_{16} branched alkane	16	1.96×10^{-11}	0.988	0.988	*n*-tetradecane	methylundecane
C_{17} branched alkane	17	2.1×10^{-11}	0.440	0.440	*n*-pentadecane	methylundecane
C_{18} branched alkane	18	2.24×10^{-11}	0.573	0.573	*n*-hexadecane	methylundecane
C_{19} branched alkane	19	2.38×10^{-11}	0.343	0.343	*n*-heptadecane	methylundecane
C_{20} branched alkane	20	2.52×10^{-11}	0.194	0.194	*n*-octadecane	methylundecane
C_{21} branched alkane	21	2.67×10^{-11}	0.128	0.128	*n*-nonadecane	methylundecane
C_{22} branched alkane	22	2.81×10^{-11}	0.121	0.121	*n*-eicosane	methylundecane
C_{12} cyclic alkane	12	1.82×10^{-11}	8.690	8.690	*n*-tetradecane	hexylcyclohexane
C_{13} cyclic alkane	13	1.68×10^{-11}	8.858	8.858	*n*-pentadecane	hexylcyclohexane
C_{14} cyclic alkane	14	1.39×10^{-11}	6.299	6.299	*n*-hexadecane	hexylcyclohexane
C_{15} cyclic alkane	15	1.82×10^{-11}	5.723	5.723	*n*-heptadecane	hexylcyclohexane
C_{16} cyclic alkane	16	1.96×10^{-11}	4.372	4.372	*n*-octadecane	hexylcyclohexane
C_{17} cyclic alkane	17	2.1×10^{-11}	3.711	3.711	*n*-nonadecane	hexylcyclohexane
C_{18} cyclic alkane	18	2.24×10^{-11}	3.382	3.382	*n*-eicosane	hexylcyclohexane
C_{19} cyclic alkane	19	2.38×10^{-11}	2.115	2.115	*n*-heneicosane	hexylcyclohexane
C_{20} cyclic alkane	20	2.52×10^{-11}	1.181	1.181	*n*-docosane	hexylcyclohexane
C_{21} cyclic alkane	21	2.67×10^{-11}	0.748	0.748	*n*-tricosane	hexylcyclohexane
C_{22} cyclic alkane	22	2.81×10^{-11}	0.629	0.629	*n*-tricosane	hexylcyclohexane
dodecane	12	1.82×10^{-11}	1.167	1.167	*n*-dodecane	*n*-dodecane
tridecane	13	1.68×10^{-11}	1.094	1.094	*n*-tridecane	*n*-dodecane
tetradecane	14	1.39×10^{-11}	0.730	0.730	*n*-tetradecane	*n*-dodecane
pentadecane	15	1.82×10^{-11}	0.613	0.613	*n*-pentadecane	*n*-dodecane
hexadecane	16	1.96×10^{-11}	0.456	0.456	*n*-hexadecane	*n*-dodecane
heptadecane	17	2.1×10^{-11}	0.331	0.331	*n*-heptadecane	*n*-dodecane
octadecane	18	2.24×10^{-11}	0.296	0.296	*n*-octadecane	*n*-dodecane
nonadecane	19	2.38×10^{-11}	0.145	0.145	*n*-nonadecane	*n*-dodecane
eicosane	20	2.52×10^{-11}	0.073	0.073	*n*-eicosane	*n*-dodecane
heneicosane	21	2.67×10^{-11}	0.044	0.044	*n*-heneicosane	*n*-dodecane
docosane	22	2.81×10^{-11}	0.029	0.029	*n*-docosane	*n*-dodecane
pristane	19	2.44×10^{-11}	0.287	0.287	*n*-nonadecane	methylundecane
phytane	20	2.61×10^{-11}	0.160	0.160	*n*-eicosane	methylundecane
naphthalene	10	2.3×10^{-11}	0.208	0.208	naphthalene	naphthalene
phenanthrene	14	1.3×10^{-11}	0.024	0.0235	naphthalene	naphthalene

929

930   **8 Figures**
931
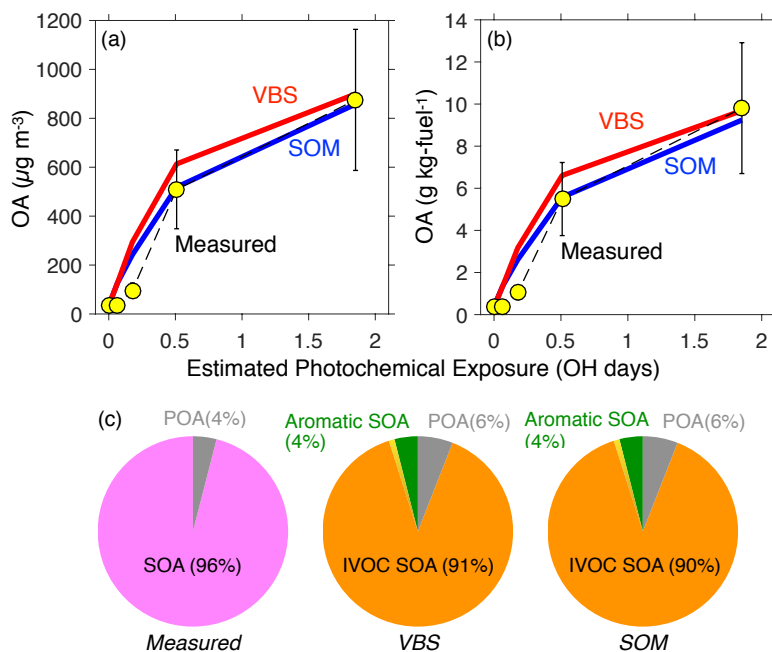
932
933   *Figure 1: VBS and SOM model predictions of OA compared to measurements from the experiment performed on June 5 (Idle-*
934   *Diesel-None) as a function of photochemical age. Inputs for both models have been specified in the text. Panel (a) has*
935   *comparisons in μg m⁻³ and panel (b) has comparisons in g kg-fuel⁻¹. Panel (c) shows the modeled and measured OA*
936   *composition at the highest photochemical exposure.*
937
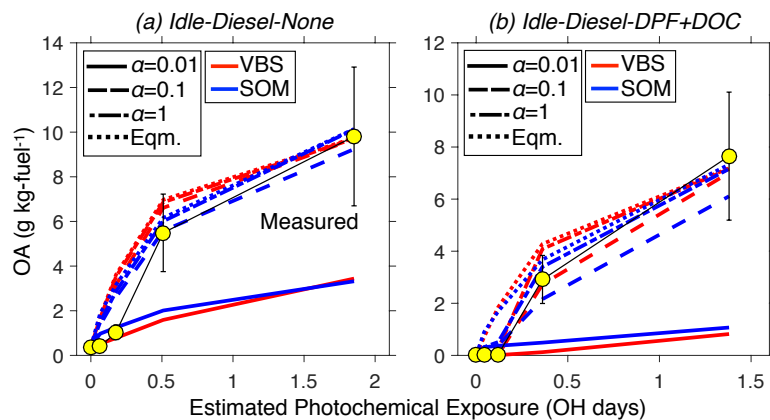
938
939   *Figure 2: VBS model predictions of OA compared to measurements from the experiment performed on June 5 (Idle-Diesel-*
940   *None) as a function of photochemical age assuming instantaneous equilibrium partitioning and kinetic gas/particle*
941   *partitioning run at three accommodation coefficients, α = 1 (dash-dot) ,0.1 (dash) and 0.01 (solid).*
942
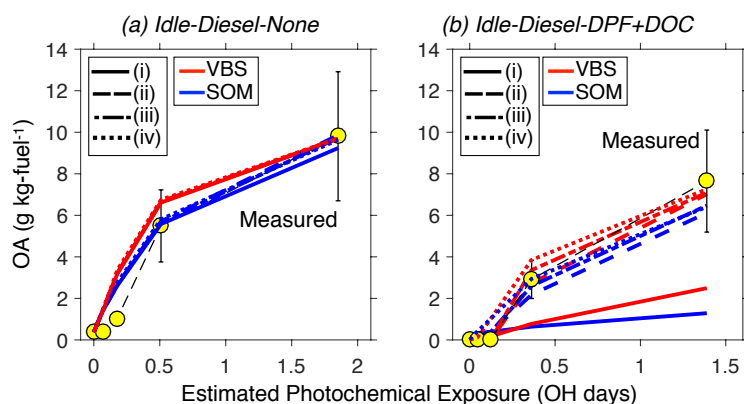
943
944 *Figure 3: VBS and SOM model predictions of OA compared to measurements from the experiments performed on (a) June 5*
945 *(Idle-Diesel-None) and (b) June 11 (Idle-Diesel-DPF+DOC) as a function of photochemical age for four different particle size*
946 *distribution inputs: (i) number mean diameter and measured number concentration at no OH exposure (solid), (ii) number*
947 *mean diameter and measured number concentration at the given OH exposure (dash), (iii) average of (i) and (ii) (dash-dot),*
948 *and (iv) nucleation of 1 nm particles (dot).*
949
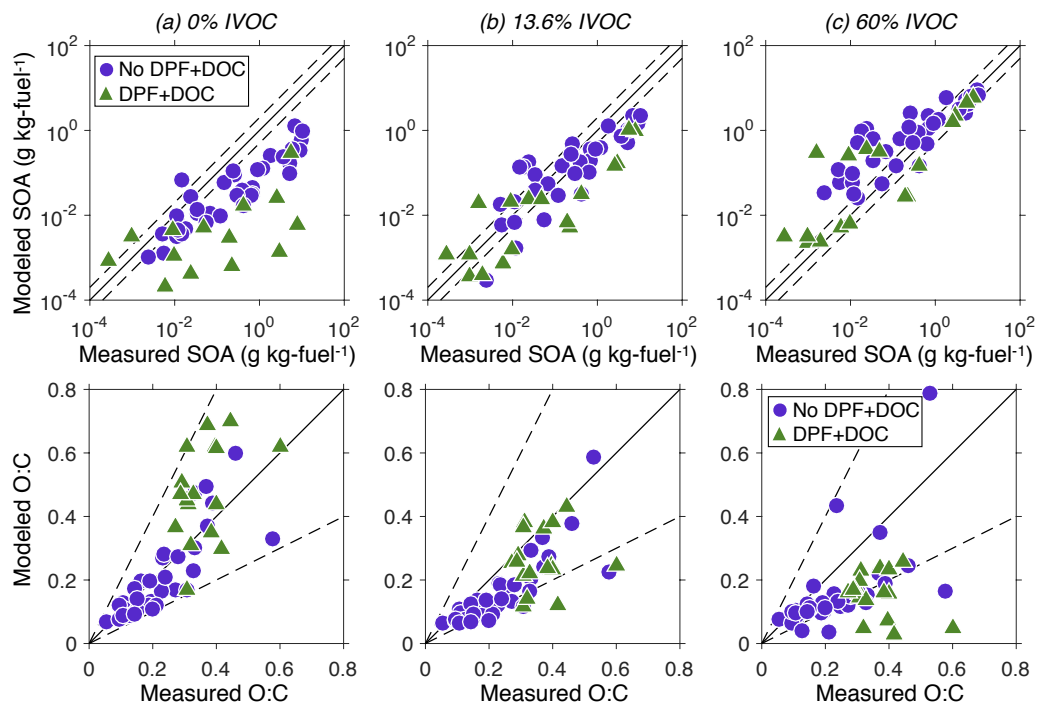
950
951 *Figure 4: Scatter plot comparing SOM predictions of OA mass and O:C to measurements from all experiments at all*
952 *photochemical ages at three different IVOC mass fractions: (a) 0%, (b) 13.76%, and (c) 60%.*
953
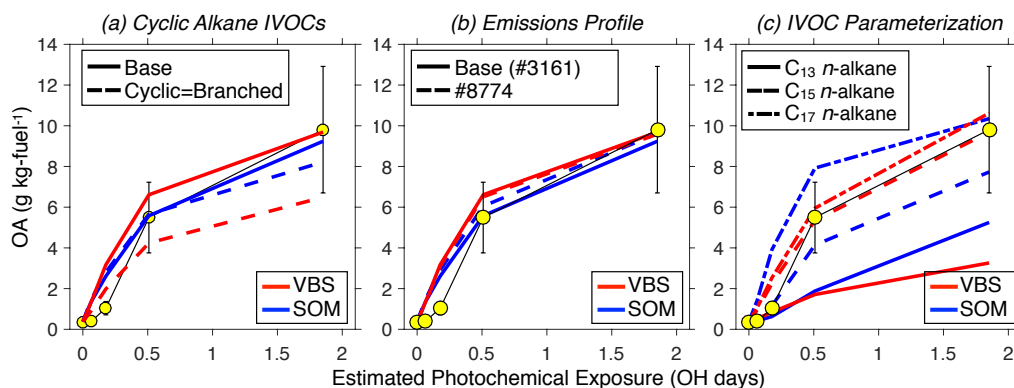
954
955 *Figure 5: VBS and SOM predictions of OA compared to measurements from the experiment performed on June 5 (Idle-Diesel-*
956 *None) as a function of photochemical age. Panel (a) examines uncertainty in model treatment of cyclic alkanes, panel (b)*
957 *examines uncertainty in the VOC emissions profile, and (c) explores suitability of using a single surrogate linear alkane to*
958 *model SOA formation from all IVOCs.*
959
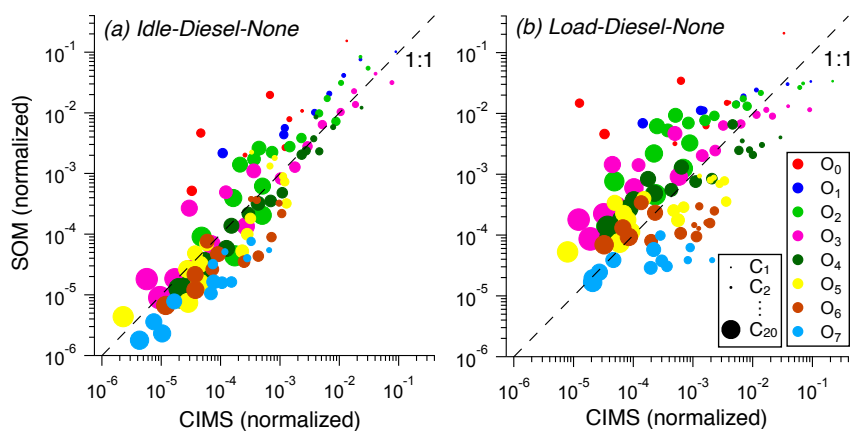
960
961 *Figure 6: Normalized gas-phase concentration predictions from the SOM model for the Idle-Diesel-None and Load-Diesel-*
962 *None experiments performed on June 5 and compared to normalized gas-phase concentrations measured by the CIMS.*
963
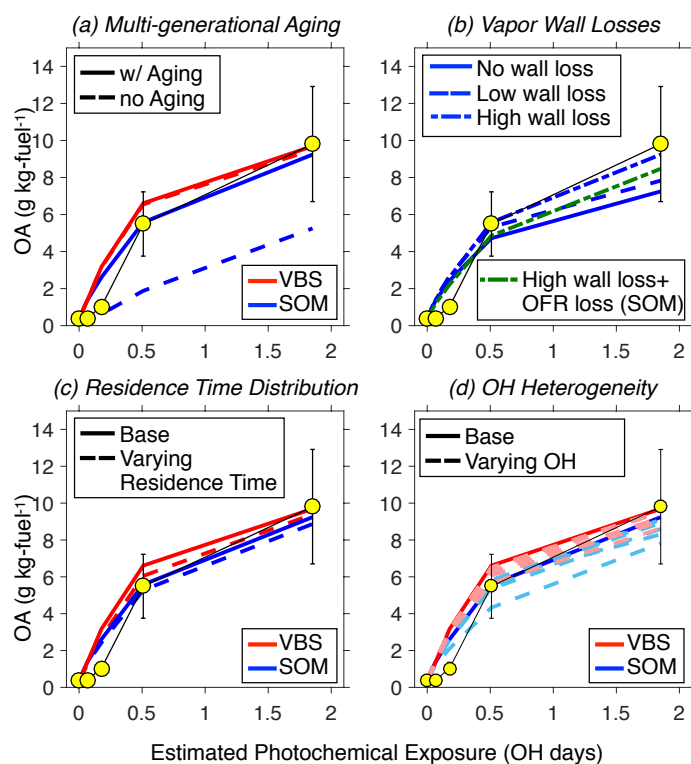
Figure 7: VBS and SOM predictions of OA compared to measurements from the experiment performed on June 5 (Idle-Diesel-None) as a function of photochemical age. Panels (a), (b), (c), and (d) examine the influence of multi-generational aging, vapor wall losses, residence time distribution, and spatial heterogeneity in OH concentrations respectively.
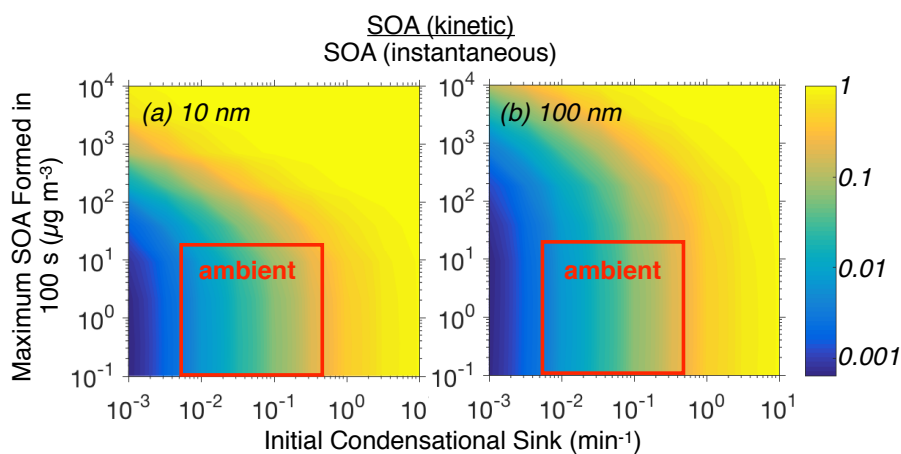
Figure 8: Model predictions of the ratio of SOA produced under kinetic partitioning assumptions to the SOA produced under instantaneous partitioning assumptions as a function of the initial condensational sink and the SOA formed under instantaneous partitioning. Panels (a) and (b) are for calculations performed at two different particles sizes: 10 and 100 nm.